Tunable spin-orbit coupling in two-dimensional InSe

A. Ceferino,[1,2,*] S. J. Magorrian,[2] V. Zólyomi,[3] D. A. Bandurin,[4,1] A. K. Geim,[1,2] A. Patanè,[5] Z. D. Kovalyuk,[6] Z. R. Kudrynskyi,[5] I. V. Grigorieva,[1,2] and V. I. Fal'ko[1,2,7]

[1]*Department of Physics and Astronomy, University of Manchester, Oxford Road, Manchester M13 9PL, United Kingdom*
[2]*National Graphene Institute, Booth Street East, Manchester M13 9PL, United Kingdom*
[3]*STFC Hartree Centre, Daresbury Laboratory, Daresbury, Warrington WA4 4AD, United Kingdom*
[4]*Department of Physics, Massachusetts Institute of Technology, Cambridge, Massachusetts 02139, USA*
[5]*School of Physics and Astronomy, University of Nottingham, Nottingham NG7 2RD, United Kingdom*
[6]*Institute for Problems of Materials Science, The National Academy of Sciences of Ukraine, Chernivtsi 58001, Ukraine*
[7]*Henry Royce Institute for Advanced Materials, Manchester M13 9PL, United Kingdom*

(Received 27 January 2021; accepted 30 June 2021; published 22 September 2021)

We demonstrate that spin-orbit coupling (SOC) strength for electrons near the conduction band edge in few-layer γ-InSe films can be tuned over a wide range. This tunability is the result of a competition between film-thickness-dependent intrinsic and electric-field-induced SOC, potentially, allowing for electrically switchable spintronic devices. Using a hybrid $\mathbf{k}\cdot\mathbf{p}$ tight-binding model, fully parametrized with the help of density functional theory computations, we quantify SOC strength for various geometries of InSe-based field-effect transistors. The theoretically computed SOC strengths are compared with the results of weak antilocalization measurements on dual-gated multilayer InSe films, interpreted in terms of Dyakonov-Perel spin relaxation due to SOC, showing a good agreement between theory and experiment.

DOI: 10.1103/PhysRevB.104.125432

I. INTRODUCTION

Indium selenide (InSe) is a layered semiconductor with already demonstrated high mobility and versatile optical properties [1–8]. Atomically thin InSe films (exfoliated from bulk crystals [9] or produced by chemical vapor deposition [10]) have already been used to fabricate field-effect transistors (FET devices). Moreover, the persistence of high mobility [11–13] of electrons in n-type doped γ-InSe to only few atomic layers [3,4,9] in thickness makes it feasible to implement InSe in spintronic devices [14]. In contrast to the conventional InAs [15] or HgTe [16,17] quantum wells, in γ-InSe it is possible to completely suppress the conduction band spin-orbit coupling (SOC) using applied displacement field, allowing for exceptionally tunable spintronic devices. One of the methods to control the electron spin in semiconductors is to manipulate its SOC [18–24] and, in this paper, we study the dependence of SOC for two-dimensional (2D) electrons near the conduction band edge of InSe films on the number of layers and on the gate-controlled electrostatic doping in the films implemented in the FET geometry [25–33].

Below, we use the earlier developed hybrid $\mathbf{k}\cdot\mathbf{p}$ tight-binding (HkpTB) model for InSe [35,36], taking into account the s and p_z orbital composition of the lowest conduction subband and self-consistent analysis of the electrostatic potential on each layer [37], and show that the dominant term in the SOC in γ-stacked InSe multilayer thin film (any number of layers) has the generic form, introduced by Thomas [38]

$$\hat{H}_{\text{SOC}} = \alpha(\mathbf{s}\times\mathbf{k})\cdot\hat{\mathbf{z}}. \tag{1}$$

This is the only linear in wave vector $\mathbf{k} = (k_x, k_y)$ of electron (in the vicinity of the Γ-point) term allowed by C_{3v} point-group symmetry of the lattice of γ-stacked multilayer (the next term in the $\mathbf{k}\cdot\mathbf{p}$ theory expansion would be of the third order [39] in k, hence, much weaker for a feasible doping of the film) [40–42]. In Eq. (1), $\mathbf{s} = (\sigma_x, \sigma_y)$ is a vector composed of Pauli matrices, and α is a layer-number-dependent factor

$$\alpha(\mathcal{E}_z, N) \approx \alpha_\infty\left(1 - \frac{\chi}{(N+2.84)^2}\right) \pm \mathcal{E}_z\aleph. \tag{2}$$

Here, $\alpha_\infty \approx 34.5$ meV Å is the value of SOC at the conduction band edge of three-dimensional (3D) bulk γ-InSe, N is the number of layers in a thin film, $\chi \approx 14.9$ accounts for the nonlinear dependence of bulk SOC on the out-of-plane momentum k_z counted from the bulk A-point band edge, at $k_A = \frac{\pi}{a_z}$. Also, $\mathcal{E}_z$ is the electric field piercing the film, and parameter $\aleph$ quantifies the Fig. 1 dependence on the electric field, as shown in the inset of Fig. 1.

The overall strength of SOC in Eq. (2) is determined by the interplay between the intrinsic lattice asymmetry of the crystal (known as Dresselhaus contribution [44,45]) and the electric-field-induced symmetry breaking (the so-called Bychkov-Rashba term [46,47]). This interplay allows for the tunability of the SOC value, both by choosing the film thickness (Nd) and by applying a displacement field in the double-gated (both top- and bottom-gated) devices. The results of our analysis are exemplified in Fig. 1, indicating

*adrian.ceferino@postgrad.manchester.ac.uk

 ©2021 American Physical Society

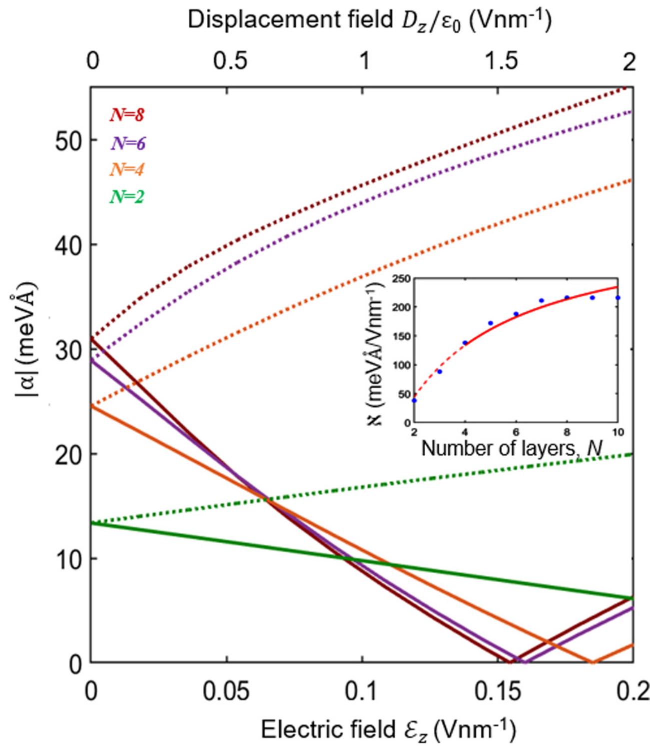

FIG. 1. SOC strength dependence on displacement field and number of layers N at $n_e = 0$ in a dual-gated FET geometry. InSe dielectric constant [34] used here is $\epsilon_z = 9.9$. The inset shows the layer-number dependence of parameter ℵ used to take into account the influence of an electric field $\mathcal{E}_z$ in Eq. (2). The solid and dotted lines indicate, respectively, when the applied displacement field suppresses or enhances the Dresselhaus SOC.

that a vertically applied electric field $\mathcal{E}_z \sim 0.15$–0.20 V nm^{-1} would be enough to switch SOC off and on, opening new avenues towards the design of spintronic devices. This form of SOC in a film is the result of $\mathbf{k}\cdot\mathbf{p}$ and tight-binding model analysis [48], parametrized using density functional theory (DFT) computations of the band structure. The theoretically calculated SOC size was compared with the values of SOC strength extracted from weak antilocalization magnetoresistance, measured in a FET based on a six-layer InSe device. We find a good agreement between theory and experiment in the available range of device parameters.

Below, the paper is organized as follows. In Sec. II, we compute the SOC coefficient in the lowest conduction subband of InSe using DFT *ab initio* calculations; in Sec. III, we perform simple perturbative calculations of SOC strength in the lowest conduction subband of bilayer InSe; and, in Sec. IV, we generalize the bilayer formalism for an arbitrary number of layers. Finally, in Sec. V, we compare the theoretically obtained SOC coefficient with the values experimentally measured in an available InSe-based FET device.

II. FIRST-PRINCIPLES CALCULATIONS OF InSe PARAMETERS

As a background to the hybrid $\mathbf{k}\cdot\mathbf{p}$ tight-binding (HkpTB) model presented in this paper, we overview the density functional theory band structure of monolayer and few-layer InSe. Monolayer InSe has pairs of vertically aligned metal atoms in the middle sublayers and chalcogens in the outer sublayers, arranged on a plane into a honeycomb structure. Such a lattice has a D_{3h} point-group symmetry which includes mirror plane symmetry, rotations by 120°, but not inversion symmetry. In any few-layer γ-InSe film, the $z \to -z$ mirror symmetry is broken. This opens a possibility for a weak "ferroelectric" charge transfer between the layers due to layer-asymmetric hybridization between the conduction and valence bands and the resulting built-in electric field in the film which may be relevant for the self-consistent analysis of the on-layer potential in a film with a finite thickness. To find out whether this is of relevance for InSe, or not, we carry out DFT calculations on a supercell with a large vacuum separating two mirror-reflected images of a γ-InSe bilayer, to satisfy periodic boundary conditions without affecting the mismatch between vacuum potentials, produced by the double-charge layer due to the charge transfer (see Fig. 2 and inset). For the DFT calculations, we used the generalized gradient approximation (GGA) of Perdew, Burke, and Ernzerhof [49], with a $12 \times 12 \times 1$ k-point grid and a plane-wave cutoff energy of 600 eV, implemented in the VASP code [50]. Monolayer atomic structure parameters, and interlayer distances, are taken from an experimental reference for the bulk crystal [43]. We find that the charge transfer between the layers is small, yielding a ≈2 meV vacuum potential difference across the bilayer in Fig. 2, which is so small that it will be neglected for the rest of the paper.

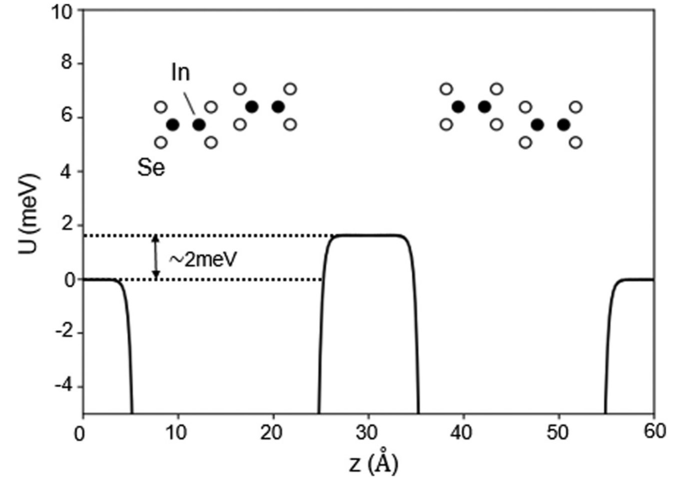

FIG. 2. Plane-averaged electrostatic potential accounting for ionic and Hartree contributions in a double-bilayer InSe supercell (supercell structure shown as inset).

Due to its mirror symmetry, the monolayer Hamiltonian cannot include s_x and s_y operators, that is, it does not display a 2D SOC. However, its symmetry allows for spin-orbit splitting in the form of [44,51]

$$\hat{H}_{\rm SO} = \gamma k^3 \sin(3\phi)\hat{s}_z, \tag{3}$$

where ϕ is the polar angle with respect to the Γ-M direction and $\hat{s}_z$ is the third Pauli matrix. This is reflected by the results of DFT computations of conduction band dispersion in monolayers, bilayers, and trilayers shown in Fig. 3.

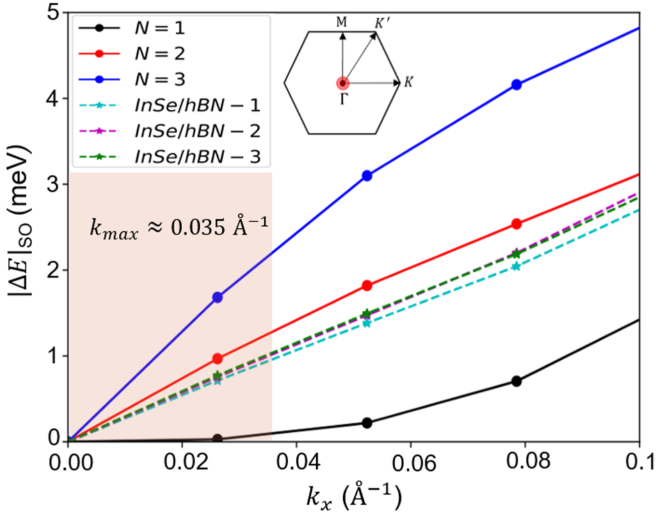

FIG. 3. DFT-calculated conduction band spin-orbit splitting for monolayer, bilayer, and trilayer InSe in for small k_x near the Γ-point. The finite thickness of the film discretizes k_z while k_x and k_y remain continuous variables. While the cubic Dresselhaus SOC splitting is expected to be zero in the Γ-M direction, in the $(k_x, 0)$ orientation a finite contribution is expected. In contrast to the orientation-dependent cubic SOC, the expected form of the linear SOC splitting [see Eq. (1)] makes this contribution isotropic in **k**. The shaded region labels the range in k_x below the Fermi level of a device doped with a carrier density of $n_e \approx 2 \times 10^{12}$ cm^{-2}. The clear linear spin splitting with k_x indicates the dominance of the linear SOC terms near the Brillouin zone (BZ) center. Also plotted using stars connected by dashed lines are values of splitting for a monolayer InSe/monolayer hBN heterostructure for three different in-plane stacking configurations. (Inset) Hexagonal BZ of monolayer InSe. The red circle indicates the region in the BZ with wave vector magnitude in the range presented.

Note that the spin polarization of the computed states is in the z direction only for monolayers, whereas for bilayers and trilayers, where it has a linear dependence announced in Eq. (1), it reflects in-plane spin splitting. In fact, for the range of in-plane wave numbers corresponding to feasible doping densities, the spin splitting in the monolayer is negligibly small [52]. We also carried out DFT calculations for a heterobilayer consisting of monolayer of InSe, and monolayer of hBN (the latter was strained to give commensurability with a lattice constant $a_{\text{hBN}} = a_{\text{InSe}}/\sqrt{3}$ and rotated to align the armchair direction of hBN with the zigzag direction of the InSe). We take the interlayer distance as 0.333 nm between the middle of hBN and the nearest plane of Se atoms. A dipole correction was applied, and we considered three in-plane configurations: (1) boron directly above indium, (2) nitrogen above indium (the hBN is inverted in-plane), and (3) configuration (1) with the hBN shifted in plane by half the B-N vector. The spin-orbit splitting near Γ in the (InSe-dominated) conduction band edge is plotted for all three configurations in Fig. 3. For the monolayer InSe/monolayer hBN heterostructure, we obtain a SOC which depends very weakly on the configuration, with a strength similar to that of the isolated InSe bilayer.

III. SPIN-ORBIT COUPLING IN InSe BILAYER

InSe belongs to the family of group-III metal-monochalcogenides with the s and p orbitals of In and Se dominating the low-energy dispersion in the vicinity of the Γ-point [35,48,51]. In the bottommost conduction band c and in the topmost valence band v, the atomic orbital composition is mainly dominated by the s and p_z orbitals of both In and Se. The deeper valence bands v_1 and v_2 are prominently Se p_x and p_y orbitals which are naturally split by the atomic SOC of the Se atoms.

In going from monolayer to bilayer γ-stacked InSe (see Fig. 4), the mirror plane symmetry is broken, reducing the symmetry from the point group D_{3h} to C_{3v}. This allows for a linear in momentum SOC splitting in the form presented in Eq. (1) prescribed by the third-order rotation symmetry axis [53]. Consequently, the interlayer hoppings need to account for the reduction of the global symmetries of the bilayer, leading to a finite Dresselhaus SOC. This appears via the interlayer mixing of the opposite z-parity bands.

We construct a bilayer Hamiltonian using monolayer Hamiltonians described in Ref. [35] taking into account interlayer hopping [35] and the intralayer interband spin-orbit coupling [54]:

$$\hat{H} = \hat{H}^{(0)} + \delta\hat{H} = \begin{pmatrix} \hat{H}_{11}^{(0)} + \delta\hat{H}_{11} & \hat{H}_{12}^{(0)} + \delta\hat{H}_{12} \\ \hat{H}_{21}^{(0)} + \delta\hat{H}_{21} & \hat{H}_{22}^{(0)} + \delta\hat{H}_{22} \end{pmatrix}. \quad (4)$$

For the analysis of SOC in the bilayer, band edge states in the constituent monolayers,

$$\Psi^{\text{T}} \equiv [c^{\uparrow}, c^{\downarrow}; c_1^{\uparrow}, c_1^{\downarrow}; v^{\uparrow}, v^{\downarrow}; v_1^{\uparrow,p_x}, v_1^{\downarrow,p_x}; v_1^{\uparrow,p_y}, v_1^{\downarrow,p_y}; v_2^{\uparrow,p_x}, v_2^{\downarrow,p_x}; v_2^{\uparrow,p_y}, v_2^{\downarrow,p_y}],$$

for the bands described in Sec. II, will be characterized by their respective band energies, neglecting an almost parabolic

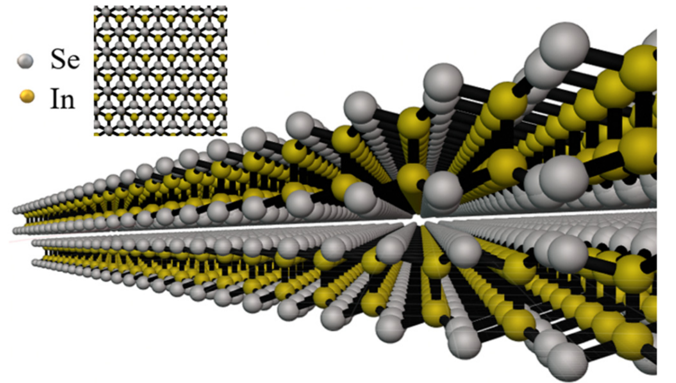

FIG. 4. Profile and top view of bilayer γ-stacked InSe. The Se atom of the top layer is shown to sit above the In atom of the bottom layer but not the other way around. This crystallographic z-asymmetry is responsible for an effective "electric field" at the origin of the Dresselhaus SOC in bilayer InSe.

band dispersion:

$$\hat{H}^{(0)}_{11(22)} = \begin{pmatrix} -U_{1(2)} & 0 & 0 & 0 & 0 \\ 0 & E_{c_1} - U_{1(2)} & 0 & 0 & 0 \\ 0 & 0 & E_v - U_{1(2)} & 0 & 0 \\ 0 & 0 & 0 & \left(E_{v_1} - U_{1(2)}\right)\hat{\mathbf{I}}_v & 0 \\ 0 & 0 & 0 & 0 & \left(E_{v_2} - U_{1(2)}\right)\hat{\mathbf{I}}_v \end{pmatrix}. \quad (5)$$

Here $\hat{\mathbf{I}}_v$ is the identity operator in the 2×2 space of atomic p_x, p_y orbital components of v_1 and v_2. $E_{c_1},\ E_v,\ E_{v_1}$, and E_{v_2} are the energy differences between the lowest conduction band and the $c_1,\ v,\ v_1$, and v_2 bands, respectively (see Fig. 5). In addition, we take into account linear in momentum interband terms in the monolayer Hamiltonian, discussed earlier in relation to the optical selection rules for the interband transitions [54]:

$$\delta\hat{H}_{11(22)} = \begin{pmatrix} 0 & 0 & 0 & ib_{54}\mathbf{k}\cdot\mathbf{\Lambda} & i\lambda_{46}(\mathbf{s}\times\mathbf{\Lambda}) \\ 0 & 0 & 0 & 0 & ib_{16}^{c_1v_2}(\mathbf{k}\cdot\mathbf{\Lambda}) \\ 0 & 0 & 0 & i\lambda_{15}(\mathbf{s}\times\mathbf{\Lambda}) & ib_{16}(\mathbf{k}\cdot\mathbf{\Lambda}) \\ -ib_{54}(\mathbf{k}\cdot\mathbf{\Lambda})^T & 0 & -i\lambda_{15}(\mathbf{s}\times\mathbf{\Lambda})^\dagger & 0 & 0 \\ -i\lambda_{46}(\mathbf{s}\times\mathbf{\Lambda})^\dagger & -ib_{16}^{c_1v_2}(\mathbf{k}\cdot\mathbf{\Lambda})^T & -ib_{16}(\mathbf{k}\cdot\mathbf{\Lambda})^T & 0 & 0 \end{pmatrix}. \quad (6)$$

Here 1×2 matrices $\mathbf{\Lambda_y} = [0, 1]$ and $\mathbf{\Lambda_x} = [1, 0]$ operate in the p_x, p_y orbital components of v_1 and v_2 valence bands and the coefficients $b_{54},\ b_{16}$, and $b_{16}^{c_1v_2}$ characterize the $c - v_1$, $v - v_2$, and $c_1 - v_2$ intralayer couplings (associated with interband optical transitions excited by the in-plane polarized photons). Spin Pauli matrices $\mathbf{s_{x,y}}$ produce spin flips upon the interband mixing which can be rooted to atomic $\mathbf{S}\cdot\mathbf{L}$ coupling (between $p_{x/y}$ and p_z orbitals which contribute to c, v, v_1, v_2 bands captured by parameters λ_{15} and λ_{46}). Note that $\mathbf{k}\cdot\mathbf{\Lambda} \equiv k_x\mathbf{\Lambda_x} + k_y\mathbf{\Lambda_y}$ and $\mathbf{s}\times\mathbf{\Lambda} \equiv \mathbf{s_x\Lambda_y} - \mathbf{s_y\Lambda_x}$.

Hopping between neighboring layers is accounted for by the following two terms:

$$\hat{H}^{(0)}_{12} = \begin{pmatrix} t^\Gamma_{cc} & 0 & 0 & 0 & 0 \\ 0 & 0 & 0 & 0 & 0 \\ 0 & 0 & t^\Gamma_{vv} & 0 & 0 \\ 0 & 0 & 0 & 0 & 0 \\ 0 & 0 & 0 & 0 & 0 \end{pmatrix}, \quad (7)$$

$$\delta\hat{H}_{12} = \begin{pmatrix} 0 & \left(t_{cc_1} + \delta_{c_1c}\right) & \left(t^\Gamma_{cv} + \delta_{cv}\right) & 0 & 0 \\ \left(-t_{cc_1} + \delta_{c_1c}\right) & 0 & 0 & 0 & 0 \\ \left(-t^\Gamma_{cv} + \delta_{cv}\right) & 0 & 0 & 0 & 0 \\ 0 & 0 & 0 & 0 & 0 \\ 0 & 0 & 0 & 0 & 0 \end{pmatrix}. \quad (8)$$

The first of them describes the resonant interlayer hybridization of separately lower conduction and the top valence band edges, which was identified [35] as the strongest hybridization effect, determined by the substantial weight of s and p_z chalcogen orbitals in the sublattice composition of the band edge states. The second term takes into account interband interlayer hybridization, which produces a much weaker effect on the band edge energies, but is sensitive to the mirror symmetry breaking set by stacking of the layers (see Fig. 5).

According to the table in Fig. 5, the on-layer states in bands c are odd under $z \to -z$ reflection while bands v and c_1 are even under the same transformation. Because of this, for a mirror-symmetric arrangement of the layers, the corresponding interband interlayer couplings would obey the relation $t^\Gamma_{cv} = -t^\Gamma_{vc}$ and $t_{c_1c} = -t_{cc_1}$. To capture the mirror plane symmetry breaking for γ-stacking, we intro-

D_{3h}	E	σ_h	$2C_3$	$2S_3$	$3C'_{2i}$	$3\sigma_{vi}$	*basis*	*orbitals*	*bands*
$A'_1(\Gamma_1)$	1	1	1	1	1	1	1	(s^+, p_z^-)	v, c_1
$A'_2(\Gamma_2)$	1	1	1	1	-1	-1	xy		
$E'(\Gamma_6)$	2	2	-1	-1	0	0	(x, y)	(p_x^+, p_y^+)	v_2
$A''_1(\Gamma_3)$	1	-1	1	-1	1	-1	xyz		
$A''_2(\Gamma_4)$	1	-1	1	-1	-1	1	z	(s^-, p_z^+)	c
$E''(\Gamma_5)$	2	-2	-1	1	0	0	(xz, yz)	(p_x^-, p_y^-)	v_1

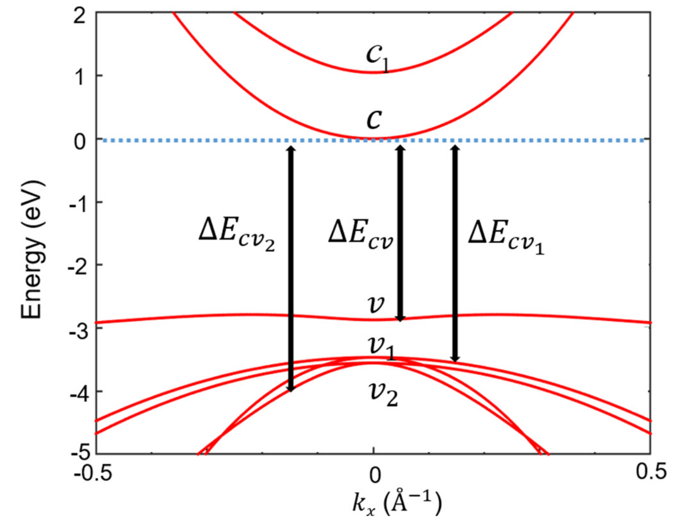

FIG. 5. (Top) Character table of the point group D_{3h} which captures the symmetries of monolayer InSe. In parentheses, the Bethe notation for each irrep is shown. Both the basis function of each irreducible representation as well as the orbital composition of any band relevant for our analysis are displayed in the final columns. The σ_h conjugacy class in the character table labels the $z \to -z$ symmetry of each irreducible representation. This crucially determines which bands are mixed due to an applied electric field. The superscripts on top of the orbitals indicate the parity with respect to the $z \to -z$ symmetry calculated in Ref. [51]. (Bottom) Band structure of monolayer InSe without SOC.

duce parameters $\delta_{\alpha\beta}$ such that $t_{cv}^{\Gamma} \to t_{cv}^{\Gamma} + \delta_{cv}$, $t_{vc}^{\Gamma} \to -t_{cv}^{\Gamma} + \delta_{cv}$, $t_{v_1v_2} \to t_{v_1v_2} + \delta_{v_1v_2}$, $t_{v_2v_1} \to -t_{v_1v_2} + \delta_{v_1v_2}$, $t_{cc_1} \to t_{cc_1} + \delta_{c_1c}$, and $t_{c_1c} \to -t_{cc_1} + \delta_{c_1c}$. Overall, the $z \to -z$ symmetry breaking in the bilayer (which gives rise to the 2D SOC in the lowest conduction subband of the bilayer) is produced by the interplay between $\delta\hat{H}_{11}$ and the contributions from $\delta_{\alpha\beta}$ in Eq. (9). For this we use third-order perturbation theory with respect to parameters δ_{c_1c}, δ_{cv}, b_{54}, b_{16}, $b_{16}^{c_1v_2}$, λ_{15}, and λ_{46}, and this results in the spin-orbit coupling constant

$$\alpha_0 = 2\left(\frac{b_{54}\lambda_{15}\delta_{cv}}{\Delta E_{cv_1}\Delta E_{g^1}} + \frac{b_{16}\lambda_{46}\delta_{cv}}{\Delta E_{cv_2}\Delta E_{g^1}} + \frac{b_{16}^{c_1v_2}\lambda_{46}\delta_{c_1c}}{\Delta E_{cc_1}\Delta E_{cv_2}}\right). \quad (9)$$

Here we also account for asymmetry induced by an external electric field so its effect on the on-layer energy of the orbitals in Eq. (5), captured by $\Delta E_{cv_1} \equiv -(t_{cc}^{\Gamma} + E_{v_1})$, $\Delta E_{cv_2} \equiv -(t_{cc}^{\Gamma} + E_{v_2})$, and $\Delta E_{cc_1} \equiv -(t_{cc}^{\Gamma} + E_{c_1})$, are the energy differences between the lowest conduction subband and v_1, v_2, and c_1 bands while $\Delta E_{g^{1(2)}} = -(t_{cc}^{\Gamma} + E_v) \pm t_{vv}^{\Gamma}$ is the energy difference between the lowest conduction subband and the first or second topmost valence subband, respectively.

In the absence of external electric field, $U_1 = U_2 = 0$, and using parameters in Table III, we estimate that $\mathcal{E}_z(\alpha_0 = 0) = 0.35\ \mathrm{V\,nm^{-1}}$. The dependence on a perpendicularly applied electric field $\mathcal{E}_z$ is approximated by

$$\aleph \equiv \left.\frac{d\alpha}{d\mathcal{E}_z}\right|_{U_1=U_2=0} = \frac{(b_{54}\lambda_{15} + b_{16}\lambda_{46})a_z t_{cv}^{\Gamma}}{\Delta E_{cv_1}} \times \left(\frac{2t_{vv}^{\Gamma}}{\Delta E_{g^1}\Delta E_{g^2}}\right)\left(\frac{1}{2t_{cc}^{\Gamma}} - \frac{1}{2t_{vv}^{\Gamma}}\right). \quad (10)$$

Here, $a_z = 8.32$ Å is the interlayer distance between the central planes of two neighboring InSe monolayers. Using parameters in Table I we estimate that for a bilayer $\aleph = 38\ \mathrm{meV\AA/V\,nm^{-1}}$, this also means that an electric field $\mathcal{E}_z = 0.35\ \mathrm{V\,nm^{-1}}$ would reduce the 2D SOC coupling strength to zero.

In addition to the above-discussed effects, mirror symmetry breaking may be caused by the encapsulation environment [55] coupling on the Se orbitals in the outer top and bottom sublayers of the crystal. This asymmetry may be due to the difference between the encapsulating materials, or even due to a different orientation of the top and bottom encapsulating layers of the same compound, e.g., hexagonal boron nitride (hBN). To describe this effect, we introduce an additional term in the bilayer Hamiltonian responsible for $c - v$, $v_1 - v_2$ band mixing with randomly different strength in the top and bottom layers

$$\delta\hat{H}_{11(22)}^{(I)} = \begin{pmatrix} \Delta E_{c1(2)} & 0 & \pm\Upsilon_{cv}^{t/b} & 0 & 0 \\ 0 & 0 & 0 & 0 & 0 \\ \pm\Upsilon_{cv}^{t/b} & 0 & \Delta E_{v1(2)} & 0 & 0 \\ 0 & 0 & 0 & \Delta E_{v_11(2)}\hat{\mathbf{I}}_\nu & \pm\Upsilon_{v_1v_2}^{t/b}\hat{\mathbf{I}}_\nu \\ 0 & 0 & 0 & \pm\Upsilon_{v_1v_2}^{t/b}\hat{\mathbf{I}}_\nu & \Delta E_{v_21(2)}\hat{\mathbf{I}}_\nu \end{pmatrix}. \quad (11)$$

Here, $\Delta E_{c1(2)}$ and $\Delta E_{v1(2)}$ are the energy shifts of the c and the v bands in the first and second layer, respectively; $\Delta E_{v_11(2)}$ and $\Delta E_{v_21(2)}$ are the energy shifts of the bands v_1 and v_2, and $\hat{\mathbf{I}}_\nu$ is the identity operator in the 2×2 space of atomic p_x, p_y orbital components of the v_1 and v_2 bands. The terms Υ_{cv}^{t} and $\Upsilon_{v_1v_2}^{t}$ are responsible for $c - v$ and $v_1 - v_2$ band mixing in the top layer: the interfacial $z \to -z$ symmetry breaking couples states of opposite parities. In the bottom surface, the interfacial effect is inverted, which is the reason for the inverted signs $-\Upsilon_{cv}^{b}$ and $-\Upsilon_{v_1v_2}^{b}$ of the corresponding terms in $\delta\hat{H}_{11(22)}^{(I)}$.

In Table II, we quote values of all those parameters obtained using DFT modeling described in Sec. II. In order to extract those parameters, the wave functions of bands c and

TABLE I. (Top) Two-band hybrid $\mathbf{k}\cdot\mathbf{p}$ tight-binding parameters extracted from the 14-band model in the bottom table. (Bottom) Hybrid $\mathbf{k}\cdot\mathbf{p}$ tight-binding model parameters used in the perturbation theory analysis. Numerical indices in the b and λ terms label the symmetry group shown in the character table in Fig. 5. The magnitude of the out-of-plane dipole moments d_{cv}, $d_{v_1v_2}$, and d_{c_1c} were obtained from the tight-binding model developed in Ref. [35]. The SOC parameter λ_{46} was calculated from the fits performed in Appendix A and the interlayer distance $a_z = 8.32$ Å was obtained from the experimental measurements shown in Ref. [43].

E_v	−2.79 eV	t_{cc}^{Γ}	0.34 eV	m_c	0.266 m_0
t_{vv}^{Γ}	−0.41 eV	t_{cc_2}	−3.43 eV Å^2	E_{v_1}	−3.4 eV
E_{v_2}	−3.5 eV	t_{cv}^{Γ}	0.25 eV	t_{cv_2}	−3.29 eV Å^2
		E_{cv}	2.79 eV		
		E_{c_1c}	1.09 eV		
		E_{vv_1}	0.54 eV		
		E_{vv_2}	0.683 eV		
		b_{54}	10.54 eV Å		
		λ_{15}	0.119 eV		
		b_{16}	−2.77 eV Å		
		$b_{16}^{c_1v_2}$	8.51 eV Å		
		d_{cv}	−1.68 eÅ		
		$d_{v_1v_2}$	−2.56 eÅ		
		d_{c_1c}	0.86 eÅ		
		t_{cc}^{Γ}	0.34 eV		
		t_{vv}^{Γ}	−0.41 eV		
		t_{cv}^{Γ}	0.25 eV		
		t_{cc_1}	0.019 eV		
		$t_{v_1v_2}$	0.048 eV		
		δ_{cv}	0.014 eV		
		δ_{c_1c}	0.022 eV		
		$\delta_{v_1v_2}$	−0.001 eV		
		λ_{46}	−0.09 eV		
		a_z	8.32 Å		

TABLE II. DFT-estimated parameters describing the effect of hBN substrate or overlay on an InSe monolayer in Eq. (11).

InSe/hBN stacking	ΔE_c	ΔE_v	$\lvert\Upsilon_{cv}\rvert$	$\lvert\Upsilon_{v_1v_2}\rvert$
1	140 meV	141 meV	35.6 meV	36.98 meV
2	155 meV	95 meV	20.5 meV	32.77 meV
3	146 meV	141 meV	35.6 meV	39.37 meV

v_1 were obtained for the three different atomic arrangements described in Sec. II. By comparing their wave-function distribution with the DFT-computed wave functions of suspended monolayer InSe, the mixing terms between opposite z-parity bands Υ_{cv} and $\Upsilon_{v_1v_2}$ were extracted for each configuration. Finally, from the DFT energy eigenvalues, the shifts in energy of bands c and v were obtained for each of the three different configurations; the energy shifts of bands v_1 and v_2 were neglected due to the very weak interlayer hybridization of those bands which results in a negligible contribution to the conduction band SOC strength. Using perturbation theory, we calculate the contribution of these additional terms towards bilayer SOC and find that the dominant effect comes from the $c-v$ band mixing, resulting in

$$\alpha^{(I)} = \left[\frac{b_{54}\lambda_{15}}{\Delta E_{g^1}\,\Delta E_{cv_1}} + \frac{b_{16}\lambda_{46}}{\Delta E_{g^1}\,\Delta E_{cv_2}}\right]\left(\Upsilon_{cv}^t - \Upsilon_{cv}^b\right). \quad (12)$$

The above equation suggests that encapsulation of InSe with the same material in the top and bottom would result in the cancellation of the main part of such an additional contribution. Due to misalignment or an offset of the encapsulating crystals, this cancellation would never be exact leaving a residual effect due to the variation of InSe and, e.g., hBN stacking. Taking into account the random nature of such a variation, in the mechanically assembled structures, we estimate characteristic size of the residual SOC contribution using the characteristic difference of the Υ_{cv} parameters for two InSe/hBN stackings analyzed in Sec. II (configurations 1 and 2 in Table II and Fig. 3). This gives $|\alpha^{(I)}| \sim 3.5$ meV Å, which is an order of magnitude smaller than $\alpha_0 = 13$ meV Å. As a result, for InSe bilayer encapsulated with hBN on both sides, the value and displacement field dependence of SOC can be well described using Eqs. (9) and (10).

IV. SPIN-ORBIT COUPLING IN MULTILAYER InSe

Here, we combine the analysis of two factors that determine the strength of SOC in multilayer γ-InSe: the asymmetry embedded into the interlayer hybridization and the effect of an externally controllable electric field.

A. Self-consistent analysis of subband electrostatics in doped multilayer InSe films

In this section, the effect of an externally applied electrostatic potential (gating) for electrons in the lowest conduction subband is calculated self-consistently, and its effect on the charge distribution and on the band gap is discussed for the dual and single-gated FET geometry as sketched in insets of Figs. 11 and 13, respectively. To quantify the SOC in the lowest conduction subband of few-layer InSe films, we describe the subband structure of the latter (both dispersion and wave functions) taking into account the electrostatic potential profile induced by doping and gating. Our "workhorse" is a two-band hybrid $\mathbf{k}\cdot\mathbf{p}$ tight-binding (HkpTB) model previously discussed in Ref. [37], formulated in the basis of conduction c and valence v band states in each layer $[c_1, v_1, c_2, v_2, \ldots]$. The HkpTB Hamiltonian has the form

$$\hat{H}^N_{\mathbf{k}\cdot\mathbf{p}} \approx \begin{pmatrix} \frac{\hbar^2k^2}{2m_c}+U_1 & 0 & t_{cc} & t_{cv} & \cdots \\ 0 & E_v+U_1 & -t_{cv} & t_{vv} & \cdots \\ t_{cc} & -t_{cv} & \frac{\hbar^2k^2}{2m_c}+U_2 & 0 & \cdots \\ t_{cv} & t_{vv} & 0 & E_v+U_2 & \cdots \\ 0 & 0 & t_{cc} & 0 & \cdots \\ \vdots & \vdots & \vdots & \vdots & \end{pmatrix}. \quad (13)$$

Here, $t_{cc(vv)}$ parametrize the interlayer conduction-conduction (valence-valence) hops ($t_{cc} \equiv t_{cc}^\Gamma + t_{cc_2}k^2$), while t_{cv} ($t_{cv} \equiv t_{cv}^\Gamma + t_{cv_2}k^2$) is the conduction to valence band hop. The zero of energy is set to the monolayer conduction band edge, so that $E_v \approx -2.8$ eV is the energy of the monolayer's topmost valence band at the Γ-point. We neglect the valence band dispersion in InSe monolayers, as earlier studies [1,56–58] have shown that it is approximately flat over a large central part of the Brillouin zone. We also neglect any k-dependence in t_{vv} for the same reason. The terms U_η account for the electrostatic potential in layer η, and they are calculated as [37]

$$U_{\eta>1} = U_1 + ea_z \sum_{\kappa=2}^{\kappa=\eta} \mathcal{E}_{(\kappa-1)\kappa}, \quad (14)$$

where $a_z = 8.32$ Å is the distance between adjacent layers and $\mathcal{E}_{(\kappa-1)\kappa}$ is the electric field between layers $\kappa-1$ and κ. $\mathcal{E}_{(\kappa-1)\kappa}$ is obtained from the electron density on each InSe layer n_η as

$$\mathcal{E}_{(\kappa-1)\kappa} = \frac{e}{\epsilon_z\varepsilon_0}\sum_{\eta=\kappa}^{\eta=N} n_\eta, \quad (15)$$

where N is the total number of InSe layers in the device, n_η is the carrier concentration at the ηth layer, and ϵ_z is the dielectric constant of InSe in the z direction. We then approximate the electric field across a single layer as the mean of the fields either side of it,

$$\mathcal{E}_\kappa \simeq (\mathcal{E}_{(\kappa-1)\kappa} + \mathcal{E}_{\kappa(\kappa+1)})/2. \quad (16)$$

Values of the parameters in the above Hamiltonian are listed in Table III. They are obtained by fitting the results of the numerical analysis of the 14-band model described in Refs. [35,37,60,61]. It is also common, in order to obtain more flexibility in gating, to have both a back gate and a top gate applied to the device as shown in the dual-gated geometry in the inset of Fig. 11. To demonstrate the behavior of the SOC coefficient in the dual-gated case, we reproduce the gating configuration used for transport experiments on a six-layer device studied in Ref. [11]. In that work, a fixed positive top gate voltage was applied to dope the system. At $V_{bg} = 0$, the carrier density in the InSe films was measured to be $n_e \sim 4\times10^{12}$ cm^{-2} indicating that the charge density

TABLE III. Dependence of the energy gap and of the effective mass of the lowest conduction subband as a function of the number of layers L; m_0 is the free-electron mass.

L	Band gap (eV)	m_c/m_0
1	2.87	0.266
2	2.14	0.220
3	1.83	0.204
4	1.67	0.197
5	1.58	0.192
6	1.52	0.189
7	1.48	0.187
8	1.46	0.186
9	1.44	0.185
10	1.42	0.184

in the top plate was that same amount. To include a fixed top gate in our electrostatic calculations, we amend Eq. (15) to read as

$$\mathcal{E}_{(\kappa-1)\kappa} = \frac{e}{\epsilon_z \varepsilon_0}\left[\sum_{\eta=\kappa}^{\eta=N} n_\eta - n_{tg}\right], \tag{17}$$

where n_{tg} is the fixed top gate carrier density and n_η the carrier density in layer η. In considering the single-gated FET geometry, a band gap modulation in the range of 10–20 meV is obtained for carrier densities in the range of 0–3 $\times$ 10^{12} cm^{-2} for 6–9 layers as shown in Fig. 6(a). Such band gap tunability [11] is a lot more efficient in the dual-gated configuration, due to a reduced electrostatic screening, with the band gap increasing up to 50 meV for an eight-layer device with a doping density of 2×10^{12} cm^{-2} and an applied top gate carrier density of $n_{tg} = 4 \times 10^{12}$ cm^{-2}. This reduction in screening also makes the charge redistribution more efficient in the dual-gated FET device compared with the single-gated configuration [see Figs. 6(b) and 6(c)].

B. SOC in multilayer films from few-layer HkpTB

In analyzing the SOC in multilayer InSe, two main mechanisms are found to determine the SOC strength. First, there are the intralayer dipole moments which mix wave functions of opposite parities within each layer under an applied electric field. Second, there is an interplay between the intrinsic inversion asymmetry of the lattice structure of γ-InSe, and the overall wave function $z \to -z$ symmetry breaking due to the applied electrostatic potential. For the analysis of SOC in multilayer InSe it is necessary to include deeper valence bands v_1 and v_2 dominated by the p_x, p_y orbitals necessary for atomic SOC mixing with the p_z orbitals in c and v (see the orbital composition of each band in the character table on top of Fig. 5). On including the deeper valence bands, the hybrid $\mathbf{k}\cdot\mathbf{p}$ tight-binding Hamiltonian $\hat{H}$ of an N-layer InSe [48] in the vicinity of the Γ-point ($k_x, k_y \to 0$) previously discussed in Sec. III is rewritten as the sum of an unperturbed $\hat{H}^{(0)}$ and a perturbative part $\delta\hat{H}$,

$$\hat{H} = \hat{H}^{(0)} + \delta\hat{H}. \tag{18}$$

Writing the wave function eigenstates of the multilayer Hamiltonian $\hat{H}$ in a $14 \times N$ band basis as $\Psi = [\Phi_1, \Phi_2, \Phi_3, \Phi_4, \ldots, \Phi_N]$, where Φ_w is the 14-band

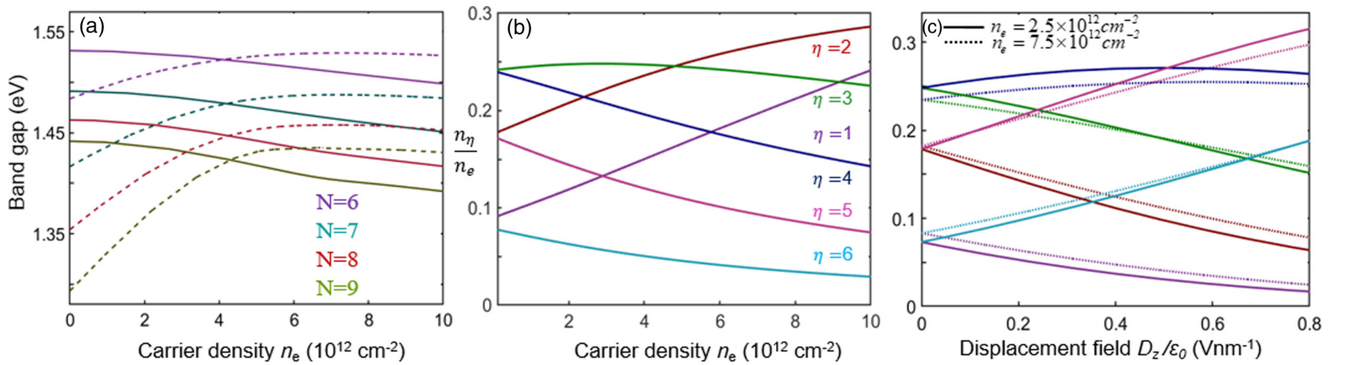

FIG. 6. (a) Band gap dependence on carrier density for a single (solid) and dual-gated (dashed) device with a fixed top gate carrier density $n_{tg} = 4 \times 10^{12}$ cm^{-2}. A reduction in the band gap with increasing electric field is expected from the displacement of electrons towards lower energies along with an increase in electrostatic energy of the holes (quantum-confined Stark effect) [8,59]. (b) Fraction of the total carrier density at each layer η in a single-gated six-layer InSe device. The first layer is defined as the one closest to the metallic gate. (c) Fraction of the total carrier density at each layer η against displacement field in a six-layer InSe device in a dual-gated configuration at two fixed carrier concentrations of $n_e = 2.5 \times 10^{12}$ cm^{-2} for the solid line and $n_e = 7.5 \times 10^{12}$ cm^{-2} for the dotted line. The same color to layer correspondence applies as in Fig. 2(b).

monolayer basis in layer w defined as

$$\Phi_w \equiv \left[c^{\uparrow(w)}, c^{\downarrow(w)}, c_1^{\uparrow(w)}, c_1^{\downarrow(w)}, v^{\uparrow(w)}, v^{\downarrow(w)}, v_1^{\uparrow,p_x(w)}, v_1^{\downarrow,p_x(w)}, v_1^{\uparrow,p_y(w)}, v_1^{\downarrow,p_y(w)}, v_2^{\uparrow,p_x(w)}, v_2^{\downarrow,p_x(w)}, v_2^{\uparrow,p_y(w)}, v_2^{\downarrow,p_y(w)}\right], \tag{19}$$

yields the following expression for $\hat{H}$, $\hat{H}_0$, and $\delta\hat{H}$:

$$\hat{H} = \begin{pmatrix} \hat{H}_{11}^{(0)} + \delta\hat{H}_{11} & \hat{H}_{12}^{(0)} + \delta\hat{H}_{12} & 0 & 0 & \cdots \\ \left(\hat{H}_{12}^{(0)} + \delta\hat{H}_{12}\right)^T & \hat{H}_{22}^{(0)} + \delta\hat{H}_{22} & \left(\hat{H}_{23}^{(0)} + \delta\hat{H}_{23}\right) & \cdots & \cdots \\ 0 & \left(\hat{H}_{23}^{(0)} + \delta\hat{H}_{23}\right)^T & \ddots & \left(\hat{H}_{(\eta-1)\eta}^{(0)} + \delta\hat{H}_{(\eta-1)\eta}\right) & \cdots \\ 0 & \vdots & \left(\hat{H}_{(\eta-1)\eta}^{(0)} + \delta\hat{H}_{(\eta-1)\eta}\right)^T & \hat{H}_{\eta\eta}^{(0)} + \delta\hat{H}_{\eta\eta} & \cdots \\ \vdots & \vdots & \vdots & \vdots & \ddots \end{pmatrix}, \tag{20a}$$

$$\hat{H}_{\eta\eta}^{(0)} = \begin{pmatrix} -U_\eta & 0 & 0 & 0 & 0 \\ 0 & (E_{c_1} - U_\eta) & 0 & 0 & 0 \\ 0 & 0 & (E_v - U_\eta) & 0 & 0 \\ 0 & 0 & 0 & (E_{v_1} - U_\eta)\hat{\mathbf{I}}_v & 0 \\ 0 & 0 & 0 & 0 & (E_{v_2} - U_\eta)\hat{\mathbf{I}}_v \end{pmatrix}, \tag{20b}$$

$$\delta\hat{H}_{\eta\eta} = \begin{pmatrix} 0 & \mathcal{E}_\eta d_{c_1c} & \mathcal{E}_\eta d_{cv} & ib_{54}\mathbf{k}\cdot\mathbf{\Lambda} & i\lambda_{46}(\mathbf{s}\times\mathbf{\Lambda}) \\ \mathcal{E}_\eta d_{c_1c} & 0 & 0 & 0 & ib_{16}^{c_1v_2}(\mathbf{k}\cdot\mathbf{\Lambda}) \\ \mathcal{E}_\eta d_{cv} & 0 & 0 & i\lambda_{15}(\mathbf{s}\times\mathbf{\Lambda}) & ib_{16}(\mathbf{k}\cdot\mathbf{\Lambda}) \\ -ib_{54}(\mathbf{k}\cdot\mathbf{\Lambda})^T & 0 & -i\lambda_{15}(\mathbf{s}\times\mathbf{\Lambda})^\dagger & 0 & \mathcal{E}_\eta d_{v_1v_2}\hat{\mathbf{I}}_v \\ -i\lambda_{46}(\mathbf{s}\times\mathbf{\Lambda})^\dagger & -ib_{16}^{c_1v_2}(\mathbf{k}\cdot\mathbf{\Lambda})^T & -ib_{16}(\mathbf{k}\cdot\mathbf{\Lambda})^T & \mathcal{E}_\eta d_{v_1v_2}\hat{\mathbf{I}}_v & 0 \end{pmatrix}, \tag{20c}$$

$$\hat{H}_{(\eta-1)\eta}^{(0)} = \begin{pmatrix} t_{cc}^\Gamma & 0 & 0 & 0 & 0 \\ 0 & 0 & 0 & 0 & 0 \\ 0 & 0 & t_{vv}^\Gamma & 0 & 0 \\ 0 & 0 & 0 & 0 & 0 \\ 0 & 0 & 0 & 0 & 0 \end{pmatrix},$$

$$\delta\hat{H}_{(\eta-1)\eta} = \begin{pmatrix} 0 & \left(t_{cc_1} + \delta_{c_1c}\right) & \left(t_{cv}^\Gamma + \delta_{cv}\right) & 0 & 0 \\ \left(-t_{cc_1} + \delta_{c_1c}\right) & 0 & 0 & 0 & 0 \\ \left(-t_{cv}^\Gamma + \delta_{cv}\right) & 0 & 0 & 0 & 0 \\ 0 & 0 & 0 & 0 & \left(t_{v_1v_2} + \delta_{v_1v_2}\right)\hat{\mathbf{I}}_v \\ 0 & 0 & 0 & \left(-t_{v_1v_2} + \delta_{v_1v_2}\right)\hat{\mathbf{I}}_v & 0 \end{pmatrix}. \tag{20d}$$

Here, indices η and κ label layers. The basis of each matrix $\hat{H}_{\eta\kappa}^{(0)}$ and $\delta\hat{H}_{\eta\kappa}$ is the 14-band monolayer InSe basis. In $\hat{H}_{\eta\eta}^{(0)}$, U_η is the electrostatic potential in the ηth layer, E_v is the monolayer topmost valence band energy as previously defined in the two-band model, E_{v_1}, E_{v_2}, and E_{c_1} are the energies of the v_1, v_2, and c_1 bands, and $\hat{\mathbf{I}}_v$ is the identity operator in the space of atomic p_x, p_y orbitals. In $\hat{H}_{(\eta-1)\eta}^{(0)}$, parameters t_{cc}^Γ and t_{vv}^Γ are the neighboring conduction-conduction (valence-valence) interlayer hoppings; no spin index has been included in Eq. (20d) and in Eq. (20b) as all nonzero matrix elements are spin independent. In $\delta\hat{H}_{(\eta-1)\eta}$, t_{cv}^Γ and δ_{cv} are the z-symmetric and z-antisymmetric $c-v$ mixing interlayer hoppings, respectively (see Appendix A). In $\delta\hat{H}_{\eta\eta}$, d_{cv}, $d_{v_1v_2}$, and d_{c_1c} are the out-of-plane dipole moments (see Fig. 5). Coefficients b_{54}, b_{16}, and $b_{16}^{c_1v_2}$ are $\mathbf{k}\cdot\mathbf{p}$ mixing terms between $c-v_1$, $v-v_2$, and c_1-v_2, respectively, while λ_{46} and λ_{15} are the atomic orbital SOC strengths for $c-v_2$ and $v-v_1$ spin-flip mixing, with values given in Table I. The latter is included using spin matrices $\mathbf{s_x}$ and $\mathbf{s_y}$. Matrices $\mathbf{\Lambda_y}$ and $\mathbf{\Lambda_x}$ are 1×2 matrices [0, 1] and [1, 0], respectively, operating in the p_x, p_y orbital component of the v_1 and v_2 valence bands and $\mathbf{k}\cdot\mathbf{\Lambda} \equiv k_x\mathbf{\Lambda_x} + k_y\mathbf{\Lambda_y}$ and $\mathbf{s}\times\mathbf{\Lambda} \equiv \mathbf{s_x}\mathbf{\Lambda_y} - \mathbf{s_y}\mathbf{\Lambda_x}$.

In the absence of interband hoppings, and having neglected the interlayer hoppings between the deeper valence bands v_1 and v_2 and between band c and the upper conduction band c_1, the subband eigenstates formed by $\hat{H}_0$ define the orthogonal basis used in the Löwdin projection. The eigenstates of the jth conduction and valence subband states in this unperturbed Hamiltonian therefore have the form $|c^j\rangle = \sum_{\eta=1}^{\eta=N}\alpha_\eta^j|c_\eta\rangle$, $|v^j\rangle = \sum_{\eta=1}^{\eta=N}\beta_\eta^j|v_\eta\rangle$, $|v_{1(2)}^j\rangle = |v_{1(2)\eta}\rangle$, $|c_1^j\rangle = |c_{1\eta}\rangle$ where $|c_\eta\rangle$, $|v_\eta\rangle$, $|v_{1(2)\eta}\rangle$, and $|c_1\rangle$ are the c, v, $v_{1(2)}$, and c_1 monolayer eigenstates in layer η, respectively. In the following analysis we will only focus on the lowest conduction subband $\alpha_\eta^1 \equiv \alpha_\eta$. For the purpose of calculating the SOC coefficient as a function of carrier density, the v_1, v_2, and c_1 subbands are approximated as all being located at $E'_{v_1} \equiv E_{v_1} - U_{av}$, $E'_{v_2} \equiv E_{v_2} - U_{av}$, and $E'_{c_1} \equiv E_{c_1} - U_{av}$, respectively, where U_{av} is the average electrostatic potential per layer. This is due to a small change in the onsite electrostatic potential $\Delta U_{(\eta-1)\eta} = U_{\eta-1} - U_\eta$, as compared with the E_{v_1},

E_{v_2}, and E_{c_1} energy denominators (0.1–0.3 eV, as compared to about 3.5 eV for c to $v_{1(2)}$ energy denominator terms and to about 1.4 eV for the c to c_1 terms). When applying the Löwdin partitioning method [62,63] (see Appendix D), the A block is chosen to act on the ↑ and ↓ spin states of the lowest conduction subband and the B block on every other subband in the InSe multiband structure.

In order to obtain the SOC term perturbatively, we account for three effects: an inversion symmetry breaking (such as an electric field or the interlayer pseudopotentials); SOC interband mixing; and $\mathbf{k}\cdot\mathbf{p}$ mixing elements. Consequently, the lowest-order nonzero terms in the perturbation theory have to be third order in the expansion. Defining

$$H'_{\rho\omega} \equiv \langle\rho|\delta\hat{H}|\omega\rangle, \tag{21}$$

where $|\rho\rangle$ and $|\omega\rangle$ are two eigenstates of $\hat{H}_0$, the corresponding third-order terms in quasidegenerate perturbation theory have the form

$$\begin{aligned}\Delta H^{(3)}_{mm'} = &-\frac{1}{2}\sum_{l,m''}\frac{H'_{ml}H'_{lm''}H'_{m''m'}}{(E_{m'}-E_l)(E_{m''}-E_l)}\\ &-\frac{1}{2}\sum_{l,m'''}\frac{H'_{mm''}H'_{m''l}H'_{lm'}}{(E_m-E_l)(E_{m''}-E_l)}\\ &+\frac{1}{2}\sum_{l,l'}\frac{H'_{ml}H'_{ll'}H'_{l'm'}}{(E_m-E_l)(E_m-E_{l'})}\\ &+\frac{1}{2}\sum_{l,l'}\frac{H'_{ml}H'_{ll'}H'_{l'm'}}{(E_{m'}-E_l)(E_{m'}-E_{l'})},\end{aligned} \tag{22}$$

where the m, m' indices correspond to $\hat{H}_0$ subband eigenstates in block A and the l, l' index to any subband eigenstate in block B (see Appendix D).

Energies $E_{m(l)}$ correspond to the energy of the mth or l^{th} eigenstate. Contributions to SOC originate from the three-step loop Feynman diagrams in Figs. 7–10, with spin-reversed initial and final states $c^{\uparrow(\downarrow)}$ and $c^{\downarrow(\uparrow)}$.

The Feynman diagrams, originating from the inversion asymmetric parameters δ_{cv} and δ_{c_1c} in combination with the mixing with deeper valence bands and SOC as shown in Figs. 7 and 8, give a term

$$\begin{aligned}\Delta H'''_{11} = 2\Bigg[&\sum_{j=1}^{j=N}\sum_{\kappa=1}^{\kappa=N}\left(\frac{b_{54}\lambda_{15}\delta_{cv}}{\Delta E_{cv_1}\Delta E_{cv^j}}+\frac{b_{16}\lambda_{46}\delta_{cv}}{\Delta E_{cv_2}\Delta E_{cv^j}}\right)\\ &\times\alpha_\kappa\left(\beta^j_{\kappa+1}+\beta^j_{\kappa-1}\right)\sum_{\xi=1}^{\xi=N}\alpha_\xi\beta^j_\xi+\sum_{\eta=1}^{\eta=N}\left(\frac{b^{c_1v_2}_{16}\lambda_{46}\delta_{c_1c}}{\Delta E_{cc_1}\Delta E_{cv_1}}\right.\\ &\left.\times\alpha_\eta(\alpha_{\eta+1}+\alpha_{\eta-1})\right)\Bigg](\mathbf{s}\times\mathbf{k}),\end{aligned} \tag{23}$$

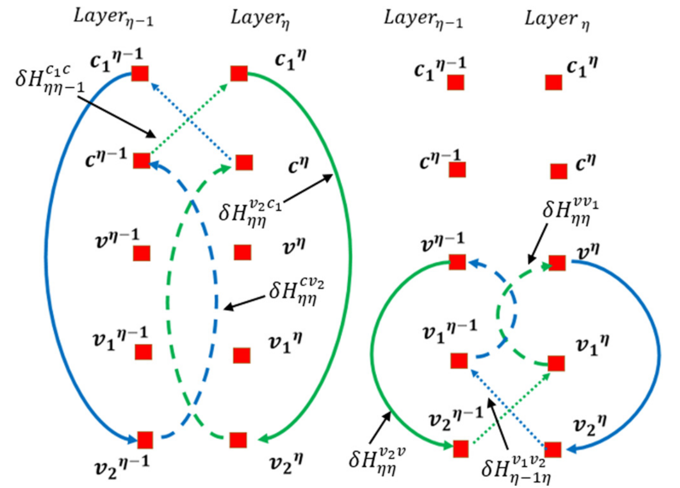

FIG. 7. (Left) Feynman diagram of the interlayer spin-flip loops due to the γ-stacking involving the upper conduction band c_1. (Right) Feynman diagram of the interlayer spin-flip loops due to the γ-stacking involving the deeper valence bands v_1 and v_2. Such contribution is only relevant for the Dresselhaus SOC in the valence band v as shown in Appendix A. Dotted lines $(\cdots)$ label the terms in $\delta\hat{H}$ responsible for inversion symmetry breaking. Dashed lines $(---)$ label the intra-atomic SOC mixing between different bands. Solid lines label the $\mathbf{k}\cdot\mathbf{p}$ interband mixing terms in $\delta\hat{H}$. Different colors label pairs of loops that produce competing contributions in the same order of perturbation theory.

where δ_{cv} and δ_{c_1c} are the z-asymmetric parameters between c and v and between c_1 and c defined in Eq. (20d) and further discussed in Appendix A. In the presence of an external electrostatic potential, the signs of δ_{cv} and δ_{c_1c} become important, as they can be related to placing a single electrostatic gate

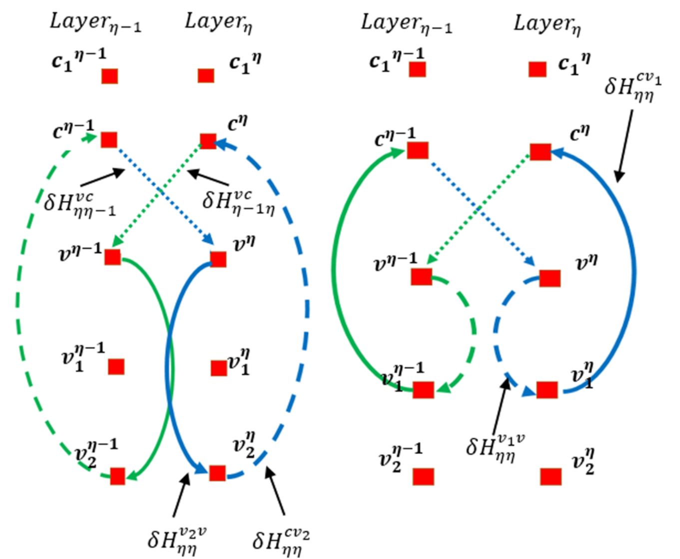

FIG. 8. Feynman diagram of the interlayer spin-flip loops due to the γ-stacking responsible for breaking the $z \to -z$ symmetry in the c to v hopping parameters t_{cv} and t_{vc}. Dotted, dashed, and solid lines follow the same convention as in Fig. 7.

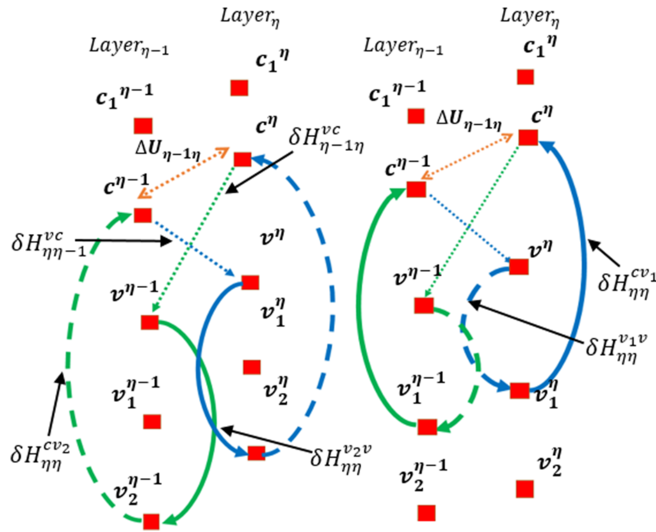

FIG. 9. Feynman diagram of the SOC originated from the asymmetry induced by the electrostatic potential distribution U_i combined with the $z \to -z$ symmetric interband hopping parameter t_{cv}. Dotted, dashed, and solid lines follow the same convention as in Fig. 7.

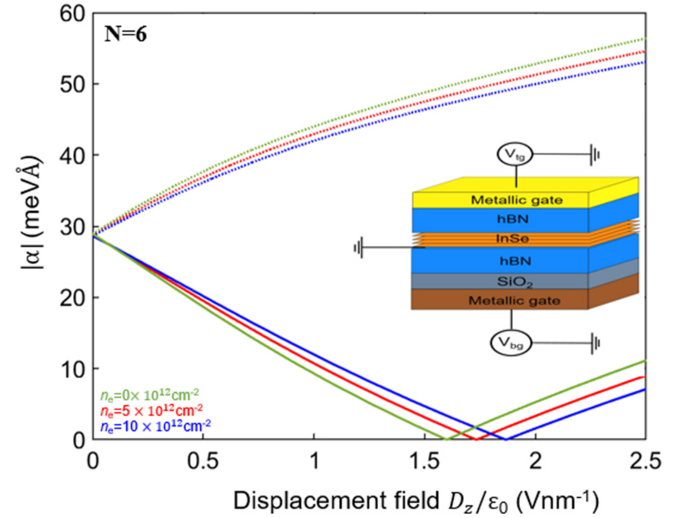

FIG. 11. SOC strength dependence on displacement field and carrier density for a six-layer InSe dual-gated FET device as shown in the inset. The solid and dotted lines indicate, respectively, when the applied displacement field suppresses or enhances the Dresselhaus SOC.

on one of the surfaces and the orientation (up or down) of externally controlled electric field $\mathcal{E}_z$.

The two diagrams in Fig. 9 give a SOC term in the form of

$$\Delta H'_{11} = 2\left[\sum_{j=1}^{j=N}\sum_{\kappa=1}^{\kappa=N}\left(\frac{b_{54}\lambda_{15}t^{\Gamma}_{cv}}{\Delta E_{cv_1}\Delta E_{cv^j}} + \frac{b_{16}\lambda_{46}t^{\Gamma}_{cv}}{\Delta E_{cv_2}\Delta E_{cv^j}}\right)\right.$$
$$\left.\times\,\alpha_\kappa\left(\beta^j_{\kappa+1} - \beta^j_{\kappa-1}\right)\left(\sum_{\xi=1}^{\xi=N}\alpha_\xi\beta^j_\xi\right)\right](\mathbf{s}\times\mathbf{k}), \quad (24)$$

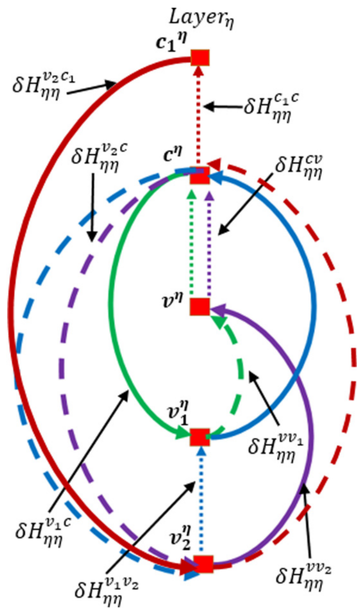

FIG. 10. Feynman diagram of the SOC from the dipolar mixing terms. Dotted, dashed, and solid lines follow the same convention as in Fig. 7. Different colors label the different three-step loops included in Eq. (22) in the same order of perturbation theory.

where α_κ and β^j_κ are the components of the lowest conduction subband and the jth valence subband, respectively; κ labels the layer index. $\Delta E_{cv^j} \equiv E_c - E_{v^j}$ is the energy difference between the lowest conduction subband and the jth valence subband and $\Delta E_{cv_{1(2)}} \equiv E_c - E'_{v_{1(2)}}$ is the energy gap between the lowest conduction subband and the v_1 and v_2 subbands located at $E_{v_{1(2)}} - U_{av}$. The loops shown in Fig. 10 for the dipolar mixing terms give a SOC term in the form of

$$\Delta H''_{11} = 2\left[\sum_{j=1}^{j=N}\sum_{\kappa=1}^{\kappa=N}\left(\frac{d_{cv}\lambda_{15}b_{54}}{\Delta E_{cv^j}\Delta E_{cv_1}} + \frac{d_{cv}\lambda_{46}b_{16}}{\Delta E_{cv^j}\Delta E_{cv_2}}\right)\right.$$
$$\times\left(\mathcal{E}_\kappa\alpha_\kappa\beta^j_\kappa\right)\left(\sum_{\xi=1}^{\xi=N}\alpha_\xi\beta^j_\xi\right) + \sum_{\eta=1}^{\eta=N}\alpha^2_\eta\mathcal{E}_\eta\times\left(\frac{d_{v_1v_2}b_{54}\lambda_{46}}{\Delta E_{cv_1}\Delta E_{cv_2}}\right.$$
$$\left.\left. + \frac{d_{c_1c}b^{c_1v_2}_{16}\lambda_{46}}{\Delta E_{cc_1}\Delta E_{cv_2}}\right)\right](\mathbf{s}\times\mathbf{k}), \quad (25)$$

where d_{cv} is the matrix element of the out-of-plane dipole operator between the monolayer conduction and valence bands, $d_{v_1v_2}$ is the out-of-plane dipole moment between v_1 and v_2 and d_{c_1c} the out-of-plane dipole between c_1 and c. $\mathcal{E}_\eta$ is defined as the electric field in layer η and $\Delta E_{cc_1} \equiv E_c - E'_{c_1}$ is the energy difference between the lowest conduction subband and the set of c_1 subbands located at $E_{c_1} - U_{av}$. In accounting for the dipolar terms, some care must be taken in choosing its sign in the few-layer case, as is further explained in Appendix B.

Combining all these contributions enables us to describe the dependence of SOC strength α on the number of layers, electric field, and doping in the film as shown in Figs. 11–13. For example, as illustrated in Fig. 12, in multilayer InSe in a single-gated FET, doping the device to carrier densities $>10^{13}$ cm^{-2} can lead to the compensation of the

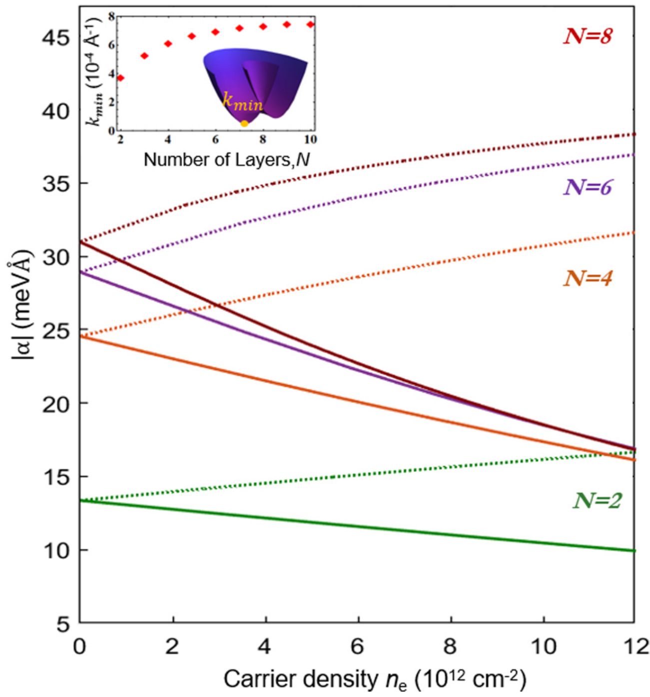

FIG. 12. 2D SOC coefficient α in the lowest conduction subband of N-layer InSe film against carrier density for different number layers in a single-gated FET geometry. Inset: shift in momentum of the minimum of the lowest conduction subband as a function of the number of layers when no electrostatic doping is present. The dielectric constant, used for this calculation, was $\epsilon_z = 9.9$. The solid and dotted lines indicate, respectively, when the applied displacement field suppresses or enhances the Dresselhaus SOC.

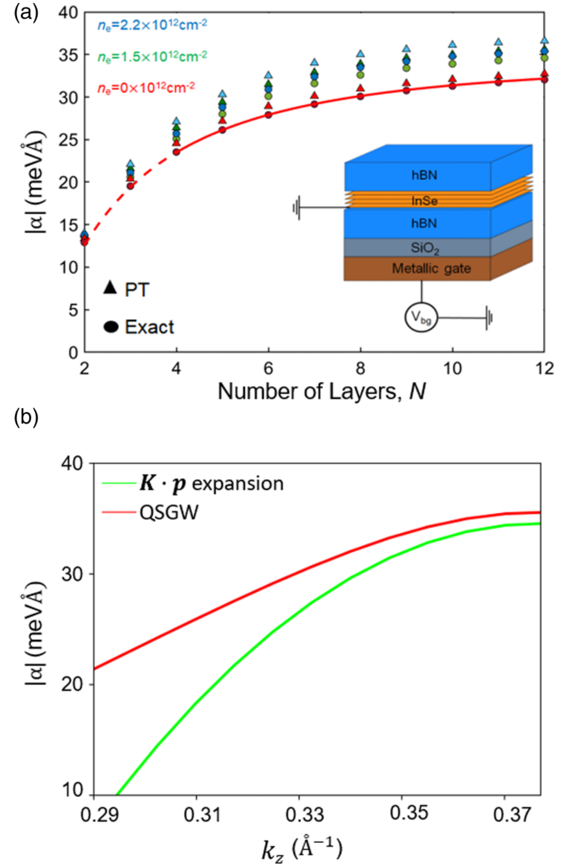

FIG. 13. (a) SOC coefficient α computed for InSe films with various thicknesses and carrier densities in a single-gated FET geometry (inset), calculated assuming $\epsilon_z = 9.9$ for the InSe. The data shown in circles (◯) were obtained by exact diagonalization of the 14-band Hamiltonian in Ref. [60] and compared with the perturbation theory results obtained by Löwdin partitioning (△) (note that for $N = 1$, $\alpha = 0$ for $n_e = 0 \times 10^{12}$ cm^{-2}). Inset shows the usual configuration of a single-gated FET device. The solid and dashed lines indicate the fitted dependence of the Dresselhaus term as a function of the number of layers when the quantum well approximation holds ($N \geqslant 4$) and when it does not, respectively. (b) In red, the QSGW-calculated SOC strength as a function of k_z in bulk γ-InSe for the conduction band [61]. As k_z approaches the band edge located at $k_z = \frac{\pi}{a_z} = 0.378$ Å^{-1}, the SOC strength increases following a quadratic dependence on wave vector p_z defined relative to the A-point as shown in green [$\alpha(p_z) = \alpha_\infty(1 - \frac{\chi a_z^2 p_z^2}{\pi^2})$, where $\alpha_\infty =$ 34.5 meV Å and $\chi = 14.9$]. This increasing trend indicates that for greater confinement under a decreasing number of layers, a weaker linear Dresselhaus SOC is expected.

intrinsic SOC by the contribution of the gate-induced electric field.

C. SOC analysis in InSe films using a quantum well model

To describe thicker films, it is more practical to use a quantum well model for InSe films [8,37]. For this, we describe the dispersion of electrons in the $\mathbf{k} \cdot \mathbf{p}$ theory expansion near the A-point conduction band edge of bulk InSe as

$$E_c(\mathbf{p}, p_z) = \left(\frac{\hbar^2}{2m_A} + \xi p_z^2 a_z^2\right)p^2 + \frac{\hbar^2 p_z^2}{2m_{Az}} + \alpha_\infty\left(1 - \frac{\chi a_z^2 p_z^2}{\pi^2}\right)(\mathbf{s} \times \mathbf{p}), \tag{26}$$

where m_A and m_{Az} are the in-plane and out-of-plane effective mass at the A-point and the parameters ξ and χ take into account the anisotropic nonparabollicity of the electron's dispersion characteristic for layered systems. In Fig. 13(b) we show the p_z dependence (around the A-point) of the linear in k_x, k_y spin-orbit coupling computed by DFT for bulk InSe using the quasiparticle self-consistent GW (QSGW) approach [60,61], to compare with the SOC form in Eq. (26). This has to be complemented with the generalized Dirichlet-Neumann boundary conditions for the quantum well wave function $\Psi(z)$ at the encapsulating interfaces

$$\Psi \pm \nu a_z \partial_z \Psi = 0, \quad \nu \approx 1.42. \tag{27}$$

The latter determines the values for the wave numbers of the electron's standing waves

$$p_z = \frac{n\pi}{(N + 2\nu)a_z}, \tag{28}$$

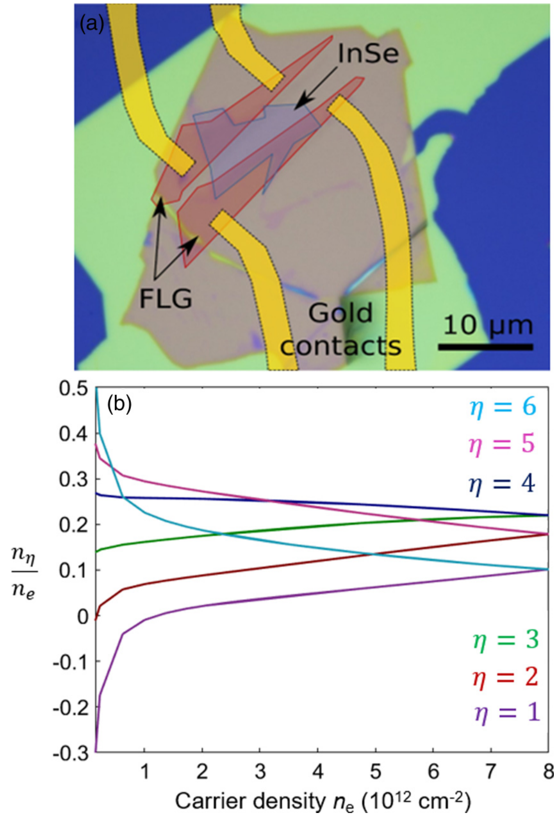

FIG. 14. (a) Optical photograph of an encapsulated InSe flake (light blue) equipped with few-layer graphene (FLG) contacts (red). Yellow polygons illustrate gold leads contacting FLG. Green color corresponds to the bottom hBN flake deposited on top of an oxidized Si wafer (dark blue). (b) Calculated charge density distribution along the different layers in the dual-gated device under study. At a carrier concentration of $n_e = 8 \times 10^{12}$ cm^{-2}, the distribution of charges becomes $z \to -z$ symmetric as the top plate carrier density is fixed at $n_{tg} = 4 \times 10^{12}$ cm^{-2}.

which determines the subband and layer-number dependence of the subband mass [37] and SOC parameter,

$$\frac{1}{m_n} \approx \frac{1}{m_A}\left(1 - \frac{6.2n^2}{(N+2\nu)^2}\right),$$

$$\alpha_{n|N}(n \ll N) \approx \alpha_\infty\left(1 - \frac{\chi n^2}{(N+2\nu)^2}\right). \quad (29)$$

By fitting $\alpha_{1|N}$ described in Eq. (2) to the values of the lowest subband SOC strength in Fig. 13 we find that $\alpha_\infty = 34.5$ meV Å and $\chi = 14.9$, respectively. Additionally, the results of the calculations, performed in the same films subjected to an electric field $\mathcal{E}_z$ perpendicular to the layers shown in Figs. 1 and 11 show an approximately linear SOC strength dependence on $\mathcal{E}_z$. We describe the latter as

$$\alpha(N, \mathcal{E}_z) = \alpha(N) \pm \mathcal{E}_z \aleph(N), \quad (30)$$

with the vales of $\aleph(N)$ for $N \geqslant 2$ shown in the inset of Fig. 1. Further to the DFT calculations for the few-layer case, in Fig. 3 we use previous QSGW calculations for bulk γ-InSe [60,61] to extract the k_z dependence of the coefficient of the linear component of SOC for small in-plane momentum near $k_x = k_y = 0$, for both the conduction and valence bands. This shows that as k_z approaches the bulk band edge (located at $k_z = \pi/a_z$) the SOC strength increases, implying that as k_z is restricted by confinement in thin films of InSe, the SOC strength can be expected to decrease from its bulk value, with smaller strengths for thinner films.

V. MAGNETOTRANSPORT STUDIES OF InSe FILMS IN THE FET GEOMETRY AND THEIR COMPARISON WITH THEORY

In order to probe the nature of SOC in InSe, we fabricated a dual-gated multiterminal six-layer γ-InSe device using mechanical exfoliation and hexagonal boron nitride (hBN) encapsulation, which were carried out in an inert at-

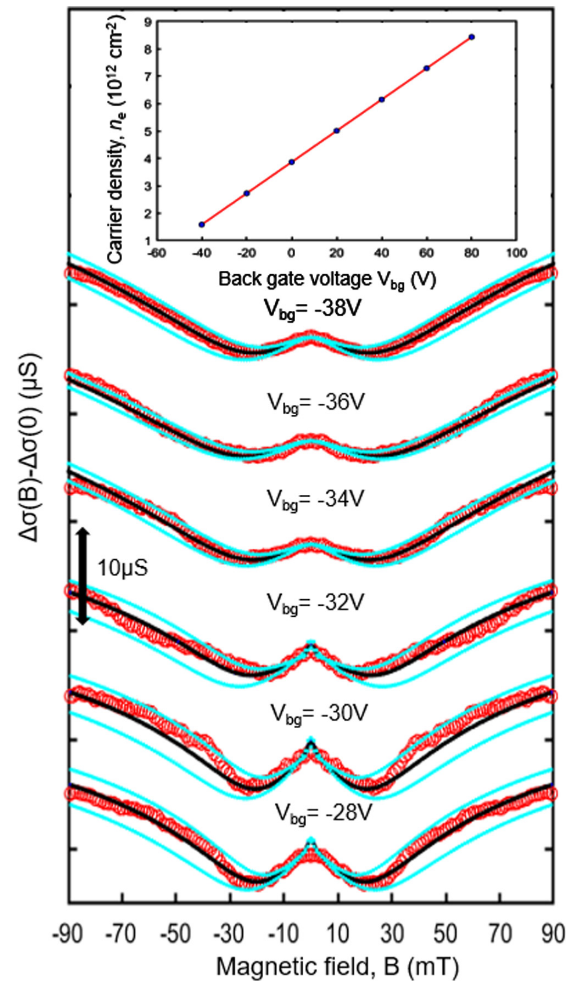

FIG. 15. Weak antilocalization feature in conductivity measured in a six-layer dual-gated InSe device with corresponding optimal fits (black). Carrier densities were measured in the range from $1.7 - 2.2 \times 10^{12}$ cm^{-2} in steps of 0.1×10^{12} cm^{-2}. Blue indicates the upper and lower bound fits of the corrections to magnetoconductivity. Top inset shows the carrier density at each back gate voltage obtained from Hall-effect measurements. The finite carrier density at $V_{bg} = 0$ is due to the applied top gate voltage corresponding to $V_{tg} = 8$ V. The linear relation between the carrier density and the back gate voltage for a fixed top gate of $V_{tg} = 8$ V was found to be $n_e = \Upsilon(V_{bg} - V'_{bg(V_{tg}=8\text{ V})})$ where $V'_{bg(V_{tg}=8\text{ V})} = -67.6$ V and $\Upsilon = 5.71 \times 10^{10}$ V^{-1} cm^{-2}.

mosphere of a glove box [64]. Such encapsulation was needed to protect air-sensitive InSe flakes from the environment [see Fig. 14(a)]. In addition, electrical contact to InSe was provided by few-layer graphene (FLG) flakes which in turn were connected to metal leads by standard nanofabrication techniques as illustrated in Fig. 14(a) (see Ref. [11] for further details). The gate-tunable work function of graphene ensured Ohmic contacts between FLG and 2D InSe [65] and thus enabled us to explore InSe properties using conventional four-terminal measurements. To characterize the fabricated device, we first measured its longitudinal resistivity ρ_{xx} as a function of gate-induced carrier density n_e. The latter was obtained via Hall-effect measurements that provided full $n_e(V_{bg})$ dependence presented in Fig. 15. In contrast to earlier studies of the quantum Hall effect in InSe/graphene interfaces [66], the perfectly linear n_e vs V_{bg} trend shown in the inset of Fig. 15 does not indicate any substantial charge transfer from the InSe to the gating surface. Using Drude formula we determined the mean-free path of charge carriers λ and respective scattering time τ, important parameters critical for further analysis. The effective mass for the lowest conduction subband used to extract τ was $m_c = 0.12m_e$, obtained from an accurate calculation of the bulk effective mass accounting both for electron-electron and electron-phonon interaction effects in the bulk conduction band [67].

An experimental manifestation of the SOC strength can be found in the weak antilocalization (WAL) corrections to magnetoconductance [68–71] produced by the interference of electron waves propagating along closed loops of random walks [72,73]. Such behavior has been observed in recent studies of few-layer single-gated GaSe [74] and InSe [75,76].

In Ref. [76], the fitting procedure used to extract the SOC strength from the corrections to magnetoconductance was the formalism developed by Hikami, Larkin, and Nagaoka [70] for systems where the spin relaxation mechanism is dominated by scattering with magnetic impurities [77,78]. As the γ-stacked phase in InSe is noncentrosymmetric and therefore the spin relaxation mechanism is expected to be Dyakonov-Perel, their extracted spin relaxation parameters from WAL fits were overestimated.

In Ref. [75] the enhancement of the SOC as compared to our estimated bulk SOC strength value at the band edge ($\alpha_\infty \approx 34$ meV Å) is a result of an impurity deposition layer formed at the interface of the suspended device; this forms a sharp potential barrier at the interface and therefore increases the SOC strength.

From our weak antilocalization measurements, the spin and phase relaxation times can be obtained by fitting the corrections to conductivity with respect to these two parameters in the range of magnetic fields where the minimum in magnetoconductance appears.

The WAL corrections to the conductivity of the six-layer device with the same characteristics as reported in Ref. [11] were measured as a function of the magnetic field with 1 mT magnetic field step. As shown in Fig. 15, at magnetic fields 10–30 mT, a clear minimum in the magnetoconductance is observed. The corrections to conductivity $\Delta\sigma(B) - \Delta\sigma(0)$ were measured in the range of 0–90 mT, and both the spin and phase relaxation time were fitted with the formalism developed by Iordanskii, Larkin, and Pitaevskii [79,80] (ILP) for systems where the lack of inversion symmetry leads to the electron's spin precessing and to relaxation by Dyakonov-Perel mechanism. Such formalism was used for carrier densities $<2 \times 10^{12}$ cm^{-2}; above that carrier densities, the assumption of the ILP formalism that the precession angle $\phi = \Omega\tau \ll 1$ (Ω being the spin precession frequency and τ the momentum relaxation time), and that the magnetic field $B \ll B_{tr}$ (where $B_{tr} \equiv \frac{\hbar}{2e\lambda^2}$ and λ is the mean-free path) breaks down. The spin precession frequency Ω is then related to the spin-orbit coupling strength α through the simple relation $\Omega = \alpha k_F$ where k_F is the Fermi momentum. In these cases, we employ the approach developed by Golub [81,82], which goes beyond the diffusion approximation for arbitrarily large precession angles and for magnetic fields comparable to the transport field B_{tr}.

For the magnetoconductance fits performed at carrier densities $n_e \geqslant 2 \times 10^{12}$ cm^{-2}, the nonbackscattering corrections to conductivity were found to be negligible, and therefore corrections to conductivity only came from the backscattering loops

$$
\begin{aligned}
\sigma_{back} &= -\frac{e^2}{2\pi^2\hbar}\left(\frac{\lambda}{l_B}\right)^2 \sum_{N'=0}^{\infty} \mathrm{Tr}\left[\hat{A}_{N'}^3(\hat{I} - \hat{A}_{N'})^{-1} - \frac{P_{N'}^3}{1 - P_{N'}}\right],\\
\hat{A}_{N'} &\equiv \begin{pmatrix} P_{N'-2} - S_{N'-2}^{(0)} & R_{N'-2}^{(1)} & S_{N'-2}^{(2)} \\ R_{N'-2}^{(1)} & P_{N'-1} - 2S_{N'-1}^{(0)} & R_{N'-1}^{(1)} \\ S_{N'-2}^{(2)} & R_{N'-1}^{(1)} & P_{N'} - S_{N'}^{(0)} \end{pmatrix},\\
P_{N'} &\equiv \frac{l_B}{\lambda}\int_0^\infty \exp\left(-\frac{l_B}{\tilde{l}}x - \frac{x^2}{2}\right) L_{N'}(x^2)dx,\\
S_{N'}^{(\mu)} &\equiv \frac{l_B}{\lambda}\sqrt{\frac{N'!}{(N'+\mu)!}}\int_0^\infty \exp\left(-\frac{l_B}{\lambda}x - \frac{x^2}{2}\right) x^\mu L_{N'}^\mu(x^2)\sin^2\left(\Omega\tau\frac{l_B}{\lambda}x\right)dx,\\
R_{N'}^{(\mu)} &\equiv \frac{l_B}{\sqrt{2}\lambda}\sqrt{\frac{N'!}{(N'+\mu)!}}\int_0^\infty \exp\left(-\frac{l_B}{\lambda}x - \frac{x^2}{2}\right) x^\mu L_{N'}^\mu(x^2)\sin\left(2\Omega\tau\frac{l_B}{\lambda}x\right)dx.
\end{aligned}
\tag{31}
$$

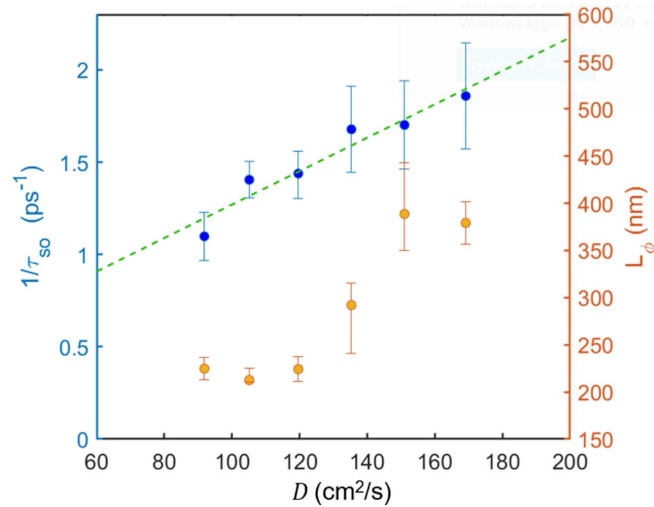

FIG. 16. Inverse spin relaxation time and phase relaxation length vs diffusion coefficient. The proportionality relation between the diffusion coefficient obtained by varying the carrier density n_e and the inverse of the spin relaxation time indicates Dyakonov-Perel mechanism of spin relaxation.

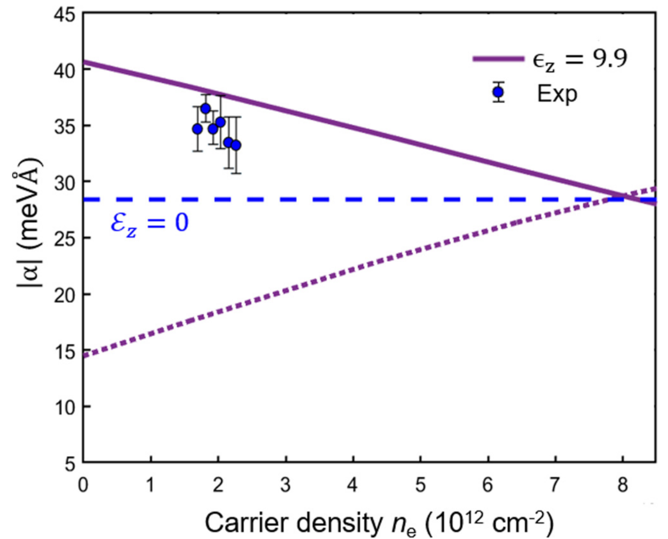

FIG. 17. SOC coefficient α as experimentally extracted from weak antilocalization measurements of the dual-gated six-layer device [11], compared to the value obtained in the self-consistent calculation. The blue dashed line indicates the value of α in the absence of any electrostatic gating and doping. The same notation for the solid and dotted lines is used as in Figs. 1, 12, and 11.

Here, $l_B \equiv \sqrt{\frac{\hbar}{eB}}$ is the magnetic length, and in Eq. (31), $\tilde{l}$ is defined as $\tilde{l} \equiv \frac{\lambda}{1+\frac{\tau}{\tau_\phi}}$ where τ_ϕ is the phase relaxation time. The precession frequency is related to the spin relaxation time τ_{SO} through $\frac{1}{\tau_{SO}} = 2\Omega^2\tau$. As done previously with the ILP formalism, both the phase and spin relaxation times were taken as fitting parameters. In Fig. 16, the inverse proportionality between the spin relaxation time and the diffusion coefficient D confirms that the spin relaxation mechanism is Dyakonov-Perel [83,84]. From τ_{SO}, the SOC coefficient is extracted and compared with our theoretical calculation in Fig. 17. In Fig. 17 the SOC coefficient at different carrier densities was calculated at the experimentally established dielectric constant $\epsilon_z = 9.9$ for InSe [34]. Very good agreement was found between the calculated SOC coefficient and the experimentally extracted SOC strength. Furthermore, by looking at the two different branches originated from the orientation of the crystal being parallel or antiparallel to the applied electric field, it was found that at a carrier density of $n_e = 8 \times 10^{12}$ cm^{-2} the two branches converged at a single point. This indicates no dependence either on crystal orientation or on electrostatic profile. As shown in Fig. 14, at that exact carrier density, the electrostatic profile is expected to be $z \to -z$ symmetric and, therefore, the only contribution to the SOC must originate from the intrinsic $z \to -z$ asymmetry of the crystal (see comparison in Fig. 17 with SOC strength at zero electric field).

VI. CONCLUSION

Overall, the description of SOC strength (as a function of the number of layers and the applied electric field piercing the multilayer film) obtained using the few-layer HkpTB study and a quantum well model give the matching results, and the theoretically computed SOC strengths are compared with the results of weak antilocalization measurements on dual-gated multilayer InSe films showing a good agreement between theory and experiment.

The size of SOC constant we compute for InSe films with 2–10 layers thickness is comparable to the SOC strength in quantum wells of conventional semiconductors, such as GaAs, InAs, HgTe. What makes 2D InSe different from those spintronic systems is that the SOC strength in it can be tuned over a wide range. Additionally, contribution originating from the asymmetry of an hBN/InSe interface was analyzed and shown to be negligible (as compared with the intrinsic SOC in the film) for InSe encapsulated in hBN both on top and in the bottom, and also to decay as N^{-3}. Moreover, we demonstrate that spin-orbit coupling strength for electrons near the conduction band edge in few-layer γ-InSe films can be tuned over a wide range, from $\alpha = 0$ to $\alpha \approx 70$ meV Å. This tunability illustrated in Fig. 18 for the films of various thicknesses is the result of a competition between film-thickness-dependent intrinsic and electric-field-induced SOC, potentially, allowing for electrically switchable spintronic devices. As shown in Figs. 18 and 1, displacement fields in the range of 1–2 V nm^{-1} can turn the SOC on and off.

ACKNOWLEDGMENTS

The authors thank M. Potemski, Y. Ye, J. Lischner, A. Mirlin, V. Enaldiev, K. W. Song, S. Slizovskiy, and N. D. Drummond for discussions. We also thank S. J. Liang and F. Miao for sharing the data in Ref. [76]. This work made use of the CSF cluster of the University of Manchester and the N8 Polaris service, the use of the ARCHER national UK supercomputer (RAP Project e547), and the Tianhe-2 Supercomputer at NUDT. We acknowledge support from EPSRC CDT Graphene NOWNANOEP/L01548X,

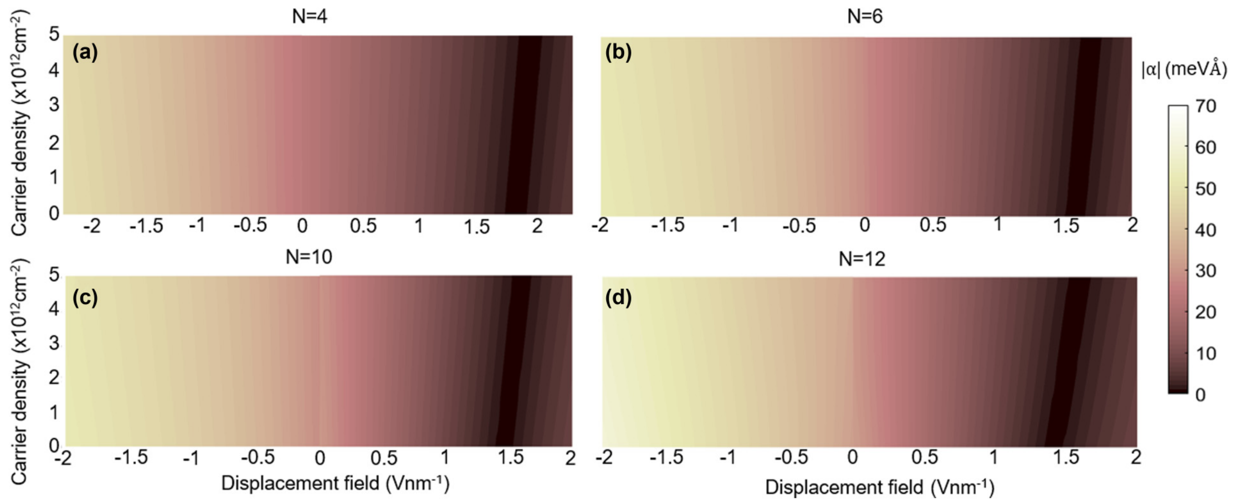

FIG. 18. (a)–(d) SOC strength as a function of the displacement field and carrier density for different number of layers. Crystal orientation is chosen such that the applied displacement field counteracts the Dresselhaus SOC when the displacement field is positive. The dark black lines indicate the disappearance of SOC due to the application of a displacement field which compensates the SOC from the intrinsic lack of inversion symmetry in the different multilayers.

ERC Synergy Grant Hetero2D, Grant No. EP/N010345, Lloyd Register Foundation Nanotechnology grant, European Quantum Technology Flagship Project 2D-SIPC, and Core 3 European Graphene Flagship Project. Research data are available from the authors on request.

APPENDIX A: DETERMINATION OF PARAMETERS δ_{cv}, δ_{c_1c}, AND $\delta_{v_1v_2}$ FROM BULK SOC

For the calculation of subband energies and dispersions, it was sufficient to approximate the interlayer hops as being entirely between the inversion symmetric sublattices of selenium atoms on the outside of each layer. This causes the hops to be inversion symmetric, which when combined with the opposite z-symmetries of the monolayer conduction and valence under σ_h reflection (i.e., $z \to -z$ symmetry) gives $t_{cv} = -t_{vc}$, $t_{c_1c} = -t_{cc_1}$, and $t_{v_2v_1} = -t_{v_1v_2}$. It is transparent from Eq. (1) that inversion symmetry would prohibit the existence of extrinsic SOC. Consequently, we require terms in our model which break inversion symmetry (such as an applied electric field or the interlayer pseudopotentials arising from the γ-stacking [85]). The indium atoms provide such an asymmetry; in the γ-stacking there is a vertically opposite interlayer In/Se pair heading in one direction along the z-direction, while in the other direction the indium atom is opposite an empty space in the adjacent layer. In the $\mathbf{k}\cdot\mathbf{p}$ model, the effect of this symmetry breaking is to give t_{cv}, t_{c_1c}, and $t_{v_1v_2}$ slightly different magnitudes as compared with $-t_{cv}$, $-t_{c_1c}$, and $-t_{v_1v_2}$, so we define three new parameters: $2\delta_{cv} \equiv t_{cv} + t_{vc}$, $2\delta_{c_1c} \equiv t_{c_1c} + t_{cc_1}$, and $2\delta_{v_1v_2} \equiv t_{v_1v_2} + t_{v_2v_1}$. In order to obtain the parameters δ_{cv} and δ_{c_1c} relevant for the analysis of the Dresselhaus SOC in the conduction band, the linear SOC splittings at each individual k_z are obtained from the QUESTAAL package by linearly fitting the energy differences between the two spin-split bands (see Fig. 19). First, the parameters δ_{cv} and δ_{c_1c} were fitted for the α vs k_z dependence of band c (red curve in Fig. 19), and then the $\delta_{v_1v_2}$ parameter was fitted from the α vs k_z dependence of band v (green curve in Fig. 19). Using the same perturbative analysis as in Sec. IV in the bulk limit, the Dresselhaus SOC at each k_z is obtained both for the c and v bands, respectively, namely,

$$\alpha_c(p_z) = 4\cos(p_z a_z)\left(\frac{\delta_{cv} b_{54}\lambda_{15}}{(E_c - E_v)(E_c - E_{v_1})} + \frac{\delta_{cv} b_{16}\lambda_{46}}{(E_c - E_v)(E_c - E_{v_2})} + \frac{\delta_{c_1c} b_{16}^{c_1v_2}\lambda_{46}}{(E_c - E_{c_1})(E_c - E_{v_2})}\right) \quad (A1)$$

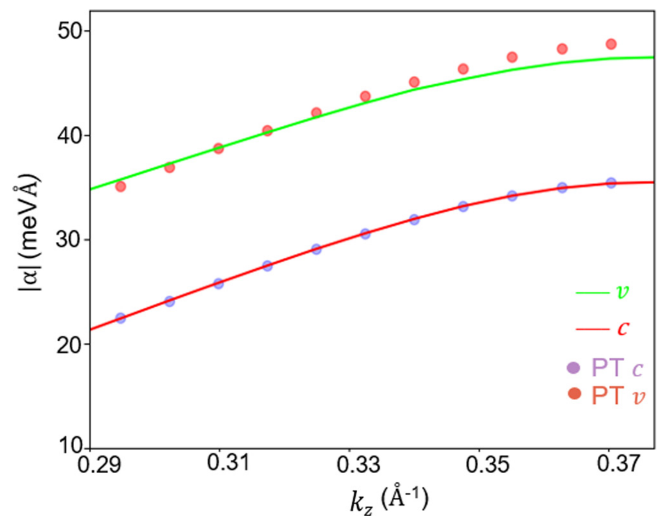

FIG. 19. (Solid) Bulk SOC as a function of k_z for c and v bands. (Dots) SOC strength at different k_z obtained from the perturbative analysis in Eqs. (A1) and (A2).

and

$$\alpha_v(p_z) = 4\cos(p_z a_z)\left(\frac{\delta_{cv} b_{54}\lambda_{15}}{(E_v - E_c)(E_v - E_{v_1})} + \frac{\delta_{cv} b_{16}\lambda_{46}}{(E_v - E_c)(E_v - E_{v_2})} + \frac{\delta_{v_1v_2} b_{16}\lambda_{15}}{(E_v - E_{v_1})(E_v - E_{v_2})}\right), \tag{A2}$$

where $p_z = \frac{\pi}{a_z} - k_z$. The fitting parameters considered are the terms δ_{cv}, δ_{c_1c}, $\delta_{v_1v_2}$, and λ_{46} as the 14-band fit applied to the InSe bulk dispersion did not account for any them. The optimal parameters found in order to fit the spin splitting vs k_z dependence in the vicinity of the band edge where perturbation theory is best applicable were $\delta_{cv} = 0.014$ eV, $\delta_{c_1c} = 0.022$ eV, $\delta_{v_1v_2} = -0.001$ eV, and $\lambda_{46} = -0.09$ eV.

APPENDIX B: DETERMINATION OF THE SIGNS OF d_{cv}, $d_{v_1v_2}$, AND d_{c_1c}

While on their own the signs of d_{cv} and t_{cv} may be chosen arbitrarily through an appropriate choice of basis in the monolayer Hamiltonian, the product of d_{cv} and t_{cv} does not have such degree of freedom. In order to determine the relative signs of the different dipole moments, it is necessary to look at their k-dependence as we move away from the Γ-point. In considering the conduction to valence band interlayer hopping (both the z-symmetric and z-antisymmetric) as a perturbation to our conduction or valence subband wave functions, the k-dependence of the bilayer valence band dipole moment follows easily as

$$\langle v_{2L}|ez|v_{2L}\rangle = 2\delta_{cv}\left[\frac{d_{cv}}{E_{g2L}} + \frac{t_{cv}ea_z}{2E_{g2L}E'_{g2L}}\right] \tag{B1}$$

for the valence band, and

$$\langle c_{2L}|ez|c_{2L}\rangle = -2\delta_{cv}\left[\frac{d_{cv}}{E_{g2L}} + \frac{t_{cv}ea_z}{2E_{g2L}E''_{g2L}}\right] \tag{B2}$$

for the bilayer conduction band. In the above equation, $d_{cv} = |\langle c|ez|v\rangle| = 1.68$ eÅ is the matrix element of the out-of-plane dipole operator between the monolayer conduction and valence bands and v_{2L} and c_{2L} are the topmost valence subband and lowest conduction subband wave functions in a bilayer system at the Γ-point. $E_{g2L} = E_c - E_v - (t_{cc} - t_{vv})$, $E'_{g2L} = E_c - E_v + t_{cc} + t_{vv}$, and $E''_{g2L} = E_c - E_v - (t_{cc} + t_{vv})$ are the energy differences between the bilayer bands in the absence of the interband hoppings. Comparison of these expressions with the signs of the quantities calculated using DFT gives, for a choice of positive t_{cv} and negative d_{cv}, a positive δ_{cv} when the $+z$ direction is chosen such that the vertical In-Se interlayer pair in the interface between two layers the Se atom lies above the In atom in the γ-stacking. Conversely, a negative δ_{cv} is obtained for the opposite orientation. On calculating perturbatively the value of d_{cv} at a finite k, the following result is obtained:

$$d_{cv}(k) \equiv \langle v|ez|c\rangle = \langle v_0|ez|c_0\rangle + \frac{b_{54}b_{16}k^2 d_{v_1v_2}}{\Delta E_{v_1c}\Delta E_{v_2v}}. \tag{B3}$$

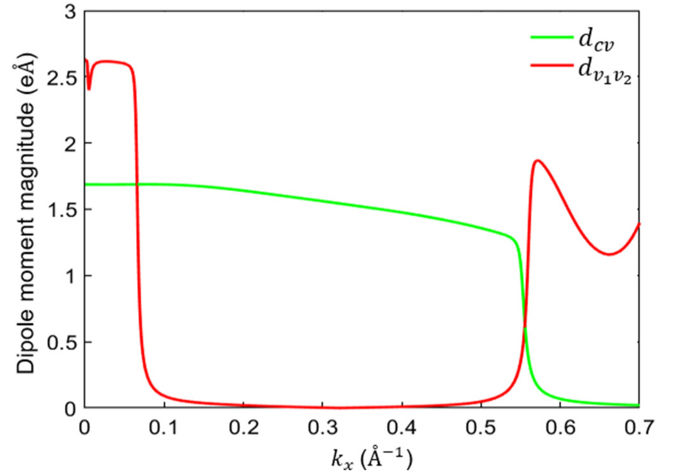

FIG. 20. Dipole moments between monolayer bands c and v (d_{cv}) and between monolayer bands v_1 and v_2 ($d_{v_1v_2}$) computed using the tight-binding model in Ref. [35].

By looking at the negative trend of $|d_{cv}|$ and the hybrid $\mathbf{k}\cdot\mathbf{p}$ tight-binding values quoted in Table III, it is transparent that if d_{cv} is positive, $d_{v_1v_1}$ is as well positive. Furthermore, if d_{cv} is negative, the value of $d_{v_1v_2}$ should be negative as well. In order to find the sign of the dipole moment d_{c_1c} a similar perturbative analysis is applied for $d_{v_1v_2}$:

$$d_{v_1v_2}(k) \equiv \langle v_1|ez|v_2\rangle = \langle v_{1,0}|ez|v_{2,0}\rangle + \frac{b_{54}b_{16}k^2 d_{cv}}{\Delta E_{v_1c}\Delta E_{v_2v}} + \frac{b_{54}b_{16}^{c_1v_2}k^2 d_{c_1c}}{\Delta E_{v_1c}\Delta E_{v_2c_1}}. \tag{B4}$$

In comparing the red and the green curves in Fig. 20, the much more pronounced steepness of the red curve as compared to the green curve at low values of k indicates that d_{c_1c} must be negative for a positive $d_{v_1v_2}$ and vice versa.

APPENDIX C: INTERFACIAL CONTRIBUTION TO MULTILAYER INSE SOC

In addition to the crystalline and the electrostatically induced $z \to -z$ asymmetry, few-layer InSe is a material sensitive to interfacial effects due to its limited thickness. Such effects may have an impact in the SOC strength of multilayer InSe and must therefore be taken into consideration [55,86,87]. The same two InSe-hBN configurations used for the analysis of interfacial effects in bilayer InSe shown in Table II (configurations 1 and 2) were also used for the calculation of the interface-induced SOC in multilayer InSe as their contribution in the absence of an external electrostatic potential is only dependent on the encapsulating substrates and on the film thickness. Interface effects are taken into account by adding into the multilayer Hamiltonian two additional contributions identical to Eq. (11). First, bands c and v with a relevant Se p_z orbital composition experience in the outer layers a shift in energy due to the interaction with the p_z orbitals of the encapsulating hBN. Therefore, an additional energy shift is added to the c, v, v_1, and v_2 bands of the first and the Nth layers.

Additionally, the hBN interfaces break $z \to -z$ symmetry in the outer layers mixing bands with opposite z-parity but identical in-plane symmetries. The following perturbative term accounting for all these effect is introduced in the multilayer Hamiltonian

$$\delta \hat{H}^{(I)}_{11(NN)} = \begin{pmatrix} \Delta E_{c1(N)} & 0 & \pm\Upsilon^{t/b}_{cv} & 0 & 0 \\ 0 & 0 & 0 & 0 & 0 \\ \pm\Upsilon^{t/b}_{cv} & 0 & \Delta E_{v1(N)} & 0 & 0 \\ 0 & 0 & 0 & \Delta E_{v_1 1(N)}\hat{\mathbf{I}}_{\nu} & \pm\Upsilon^{t/b}_{v_1 v_2}\hat{\mathbf{I}}_{\nu} \\ 0 & 0 & 0 & \pm\Upsilon^{t/b}_{v_1 v_2}\hat{\mathbf{I}}_{\nu} & \Delta E_{v_2 1(N)}\hat{\mathbf{I}}_{\nu} \end{pmatrix}, \tag{C1}$$

where Υ^{t}_{cv} and $\Upsilon^{t}_{v_1 v_2}$ are the mixing terms between bands $c - v$ and $v_1 - v_2$ in the top interface and $-\Upsilon^{b}_{cv}$, $-\Upsilon^{b}_{v_1 v_2}$ are ones mixing bands $c - v$ and $v_1 - v_2$ at the bottom interface. Note that such mixing terms require an opposite sign due to the opposite sign due to the opposite direction of the interfacial effective electric fields at the two InSe/hBN interfaces. Given the very small interfacial energy shift of bands c and v and the very weak hybridization between bands v_1 and v_2, the dominant contribution to the conduction band SOC strength originates from the interfacial terms mixing bands of opposite parity (see Fig. 21).

Among them, the most relevant contribution originates from the term Υ_{cv} mixing bands c and v, which, in the absence of an applied electric field, yield to the following contribution to the SOC strength:

$$\Delta H^{(I)}_{11} = 2\left(\left[\frac{b_{54}\lambda_{15}}{\Delta E_{g^1}\,\Delta E_{cv_1}} + \frac{b_{16}\lambda_{46}}{\Delta E_{g^1}\,\Delta E_{cv_2}}\right]\left(\Upsilon^{t}_{cv}\alpha_1\beta_1 - \Upsilon^{b}_{cv}\alpha_N\beta_N\right)\right)(\mathbf{s}\times\mathbf{k}), \tag{C2}$$

where ΔE_{g^1} is the energy between the lowest conduction subband and the topmost valence band (i.e., the energy gap) and $\Delta E_{cv_{1(2)}}$ is the energy difference between the lowest conduction subband and the $v_{1(2)}$ subbands. The number of layers dependence of the interfacial SOC strength can be extracted expanding ΔE_{g^1}, $\Delta E_{cv_{1(2)}}$, $\alpha_{1(N)}$, and $\beta_{1(N)}$ as a function of the number of layers in the quantum well approximation presented in Ref. [37]. In such approximate framework, the out-of-plane wave vector k_z depends on the number of layers as $k_z = \frac{\pi}{a_z} + \frac{n\pi}{(N+2\nu)a_z}$ and the wave functions for both the conduction and the valence bands are approximated as the eigenstates of a quantum well size $L = (N + 2\nu)a_z$ [$\Phi^1_c \approx \Phi^1_v \approx \sqrt{\frac{2}{(N+2\nu)a_z}}\cos\left(\frac{\pi z}{(N+2\nu)a_z}\right)$]. From this quantum well model, a $\frac{1}{(N+2\nu)^3}$ dependence of the interfacial SOC strength is expected, as confirmed by the fit presented in Fig. 22. Given the smallness of the interfacial SOC strength

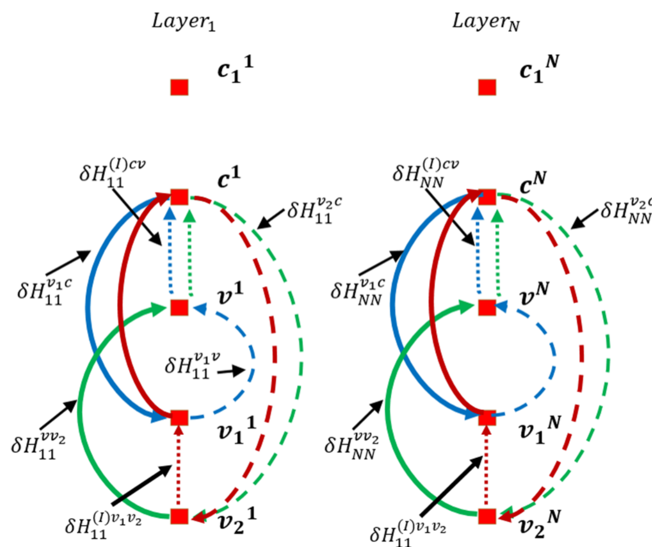

FIG. 21. Feynman diagram of the interlayer spin-flip loops due to the interfacial electric fields experienced by the electrons in the outer Se orbitals of the first and N^{th} layers. Dotted, dashed, and solid lines follow the same convention as in Fig. 7.

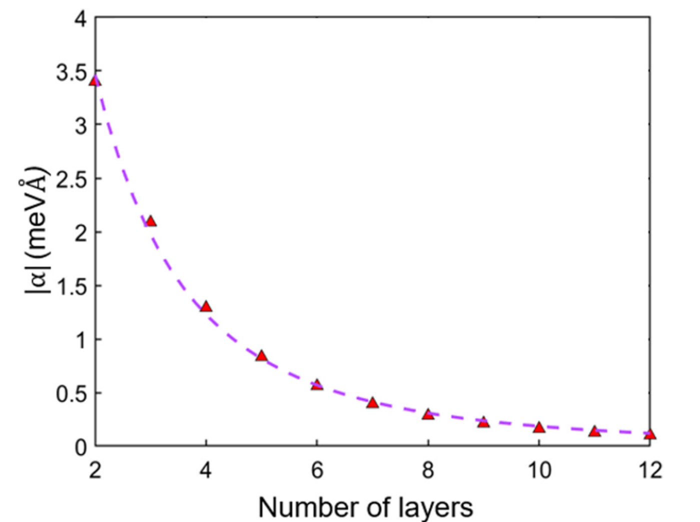

FIG. 22. Interfacial SOC as a function of the number of layers in the absence of an externally applied electric field $\mathcal{E}_z$. (Dashed) Fit of the interfacial SOC strength as a function of the number of layers. A $\frac{1}{(N+2\nu)^3}$ dependence is expected from the quantum well model presented in Ref. [37].

compared to the layer-number-dependent Dresselhaus SOC, any contribution coming from the hBN/InSe interface will be neglected for the rest of our analysis.

APPENDIX D: LÖWDIN PARTITIONING METHOD

In order to obtain the third-order corrections to the hybrid $\mathbf{k}\cdot\mathbf{p}$ tight-binding Hamiltonian, the standard method of Löwdin partitioning [62] is applied. The total multilayer Hamiltonian is written in the basis of the unperturbed subband eigenstates obtained from diagonalizing the $\hat{H}_0$ part of the Hamiltonian in Eq. (20b),

$$\hat{H} = \hat{H}_0 + \hat{H}', \tag{D1}$$

where $\hat{H}'$ is the perturbative part, namely, the projection of $\delta\hat{H}$ in the orthogonal subband basis formed by $\hat{H}_0$ ($H'_{\rho\omega} \equiv \langle\rho|\delta\hat{H}|\omega\rangle$). In the partitioning method, two diagonal blocks are defined A and B and a unitary transformation is applied to the entire Hamiltonian matrix in order to remove the nonblock-diagonal elements. The set A is defined as the elements within the lowest conduction subband c^1,

$$\hat{H}_A = \begin{pmatrix} \langle c^{1\uparrow}|\hat{H}_A|c^{1\uparrow}\rangle & \langle c^{1\uparrow}|\hat{H}_A|c^{1\downarrow}\rangle \\ \langle c^{1\downarrow}|\hat{H}_A|c^{1\uparrow}\rangle & \langle c^{1\downarrow}|\hat{H}_A|c^{1\downarrow}\rangle \end{pmatrix}, \tag{D2}$$

while the set B are the matrix elements within the valence subbands or the upper conduction subbands,

$$\hat{H}_B = \begin{pmatrix} \langle v^{1\uparrow}|\hat{H}_B|v^{1\uparrow}\rangle & \langle v^{1\uparrow}|\hat{H}_B|v^{1\downarrow}\rangle & \langle v^{1\uparrow}|\hat{H}_B|v^{2\uparrow}\rangle & \langle v^{1\uparrow}|\hat{H}_B|v^{2\downarrow}\rangle \dots \\ \langle v^{1\downarrow}|\hat{H}_B|v^{1\uparrow}\rangle & \langle v^{1\downarrow}|\hat{H}_B|v^{1\downarrow}\rangle & \langle v^{1\downarrow}|\hat{H}_B|v^{2\uparrow}\rangle & \langle v^{1\downarrow}|\hat{H}_B|v^{2\downarrow}\rangle \dots \\ \langle v^{2\uparrow}|\hat{H}_B|v^{1\uparrow}\rangle & \langle v^{2\uparrow}|\hat{H}_B|v^{1\downarrow}\rangle & \langle v^{2\uparrow}|\hat{H}_B|v^{2\uparrow}\rangle & \langle v^{2\uparrow}|\hat{H}_B|v^{2\downarrow}\rangle \dots \\ \langle v^{2\downarrow}|\hat{H}_B|v^{1\uparrow}\rangle & \langle v^{2\downarrow}|\hat{H}_B|v^{1\downarrow}\rangle & \langle v^{2\downarrow}|\hat{H}_B|v^{2\uparrow}\rangle & \langle v^{2\uparrow}|\hat{H}_B|v^{2\uparrow}\rangle \dots \\ \vdots & \vdots & \vdots & \vdots \end{pmatrix}, \tag{D3}$$

where the numerical indices such as 1 and 2 refer to the first or second subbands. The nonblock-diagonal elements H_{nbd} are the elements mixing the terms of the A and B blocks, namely,

$$\hat{H}_{nbd} = \begin{pmatrix} \langle c^{1\uparrow}|\hat{H}|v^{1\uparrow}\rangle & \langle c^{1\uparrow}|\hat{H}|v^{1\downarrow}\rangle & \langle c^{1\uparrow}|\hat{H}|v^{2\uparrow}\rangle & \dots \\ \langle c^{1\downarrow}|\hat{H}|v^{1\uparrow}\rangle & \langle c^{1\downarrow}|\hat{H}|v^{1\downarrow}\rangle & \langle c^{1\downarrow}|\hat{H}|v^{2\uparrow}\rangle & \dots \end{pmatrix}. \tag{D4}$$

The expression in Eq. (D1) is rewritten in terms of $\hat{H}'_1$ (the matrix containing the perturbations within blocks A and B) and $\hat{H}'_2$ (the nonzero perturbations between sets A and B):

$$\hat{H} = \hat{H}_0 + \hat{H}'_1 + \hat{H}'_2. \tag{D5}$$

Transforming the Hamiltonian with a unitary transformation of the form $e^{\hat{S}}$,

$$\tilde{H} = e^{-\hat{S}}\hat{H}e^{\hat{S}}, \tag{D6}$$

the deeper valence band states are projected into the lowest conduction subband. From the definition of the A block, the matrix elements $\langle c^{1\uparrow}|\hat{H}|c^{1\downarrow}\rangle$ and $\langle c^{1\downarrow}|\hat{H}|c^{1\uparrow}\rangle$ are the terms responsible for the SOC splitting. We get the following expressions for the block and nonblock-diagonal matrix elements:

$$\begin{aligned} \hat{H}_{bd} &= \sum_{j=0}^{\infty}\frac{1}{(2j)!}[\hat{H}^{(0)}+\hat{H}^{(1)},\hat{S}]^{(2j)} + \sum_{j=0}^{\infty}\frac{1}{(2j+1)!}[\hat{H}^{(2)},\hat{S}]^{(2j+1)}, \\ \hat{H}_{nbd} &= \sum_{j=0}^{\infty}\frac{1}{(2j+1)!}[\hat{H}^{(0)}+\hat{H}^{(1)},\hat{S}]^{(2j+1)} + \sum_{j=0}^{\infty}\frac{1}{(2j)!}[\hat{H}^{(2)},\hat{S}]^{(2j)}. \end{aligned} \tag{D7}$$

The nonblock-diagonal terms are then set to 0, forcing the third order in the perturbation Hamiltonian ($\Delta H^{(3)}$) to be

$$\begin{aligned} \Delta H^{(3)}_{mm'} = &-\frac{1}{2}\sum_{l,m''}\left[\frac{H'_{ml}H'_{lm''}H'_{m''m'}}{(E_{m'}-E_l)(E_{m''}-E_l)} + \frac{H'_{mm''}H'_{m''l}H'_{lm'}}{(E_m-E_l)(E_{m''}-E_l)}\right] \\ &+\frac{1}{2}\sum_{l,l'}\left[\frac{H'_{ml}H'_{ll'}H'_{l'm'}}{(E_m-E_l)(E_m-E_{l'})} + \frac{H'_{ml}H'_{ll'}H'_{l'm'}}{(E_{m'}-E_l)(E_{m'}-E_{l'})}\right], \end{aligned} \tag{D8}$$

where (m, m') are elements within A and (l, l') are elements within B. Having identified the loops responsible for the SOC splitting shown in Figs. 7–9 and 10, the mixing between the conduction and the deeper valence bands projected into the lowest

conduction subband has the form

$$\Delta H_{11}^{(3)} = 2\sum_{j=1}^{j=N}\sum_{\eta=1}^{\eta=N} \frac{\langle c^{\downarrow}|\delta\hat{H}|v_{2,\eta}^{\uparrow}\rangle\langle v_{2,\eta}^{\uparrow}|\delta\hat{H}|v^{j,\uparrow}\rangle\langle v^{j,\uparrow}|\delta\hat{H}|c^{\uparrow}\rangle}{\Delta E_{cv_2}\Delta E_{cv^j}} + 2\sum_{j=1}^{j=N}\sum_{\eta=1}^{\eta=N} \frac{\langle c^{\downarrow}|\delta\hat{H}|v_{1,\eta}^{\downarrow}\rangle\langle v_{1,\eta}^{\downarrow}|\delta\hat{H}|v^{j,\uparrow}\rangle\langle v^{j,\uparrow}|\delta\hat{H}|c^{\uparrow}\rangle}{\Delta E_{cv_1}\Delta E_{cv^j}}$$
$$+ 2\sum_{\eta=1}^{\eta=N} \frac{\langle c^{\downarrow}|\delta\hat{H}|v_{2,\eta}^{\uparrow}\rangle\langle v_{2,\eta}^{\uparrow}|\delta\hat{H}|v_{1,\eta}^{\uparrow}\rangle\langle v_{1,\eta}^{\uparrow}|\delta\hat{H}|c^{\uparrow}\rangle}{\Delta E_{cv_1}\Delta E_{cv_2}} + 2\sum_{\eta=1}^{\eta=N} \frac{\langle c^{\downarrow}|\delta\hat{H}|c_{1,\eta}^{\downarrow}\rangle\langle c_{1,\eta}^{\downarrow}|\delta\hat{H}|v_{2,\eta}^{\downarrow}\rangle\langle v_{2,\eta}^{\downarrow}|\delta\hat{H}|c^{\uparrow}\rangle}{\Delta E_{cc_1}\Delta E_{cv_2}}. \quad \text{(D9)}$$

Knowing the origin of the three-step loop processes described in Sec. IV, the Hamiltonian that contributes to the SOC in the absence of a relevant interfacial term can be decomposed as

$$\Delta H_{11}^{(3)} = \Delta H_{11}' + \Delta H_{11}'' + \Delta H_{11}''', \quad \text{(D10)}$$

where the different terms correspond to the different mechanisms behind SOC in band c:

$$\Delta H_{11}' = 2\Bigg[\sum_{j=1}^{j=N}\sum_{\kappa=1}^{\kappa=N}\left(\frac{b_{54}\lambda_{15}t_{cv}^{\Gamma}}{\Delta E_{cv_1}\Delta E_{cv^j}} + \frac{b_{16}\lambda_{46}t_{cv}^{\Gamma}}{\Delta E_{cv_2}\Delta E_{cv^j}}\right)\alpha_\kappa\left(\beta_{\kappa+1}^j - \beta_{\kappa-1}^j\right)\left(\sum_{\xi=1}^{\xi=N}\alpha_\xi\beta_\xi^j\right)\Bigg](\mathbf{s}\times\mathbf{k}),$$

$$\Delta H_{11}'' = 2\Bigg[\sum_{j=1}^{j=N}\sum_{\kappa=1}^{\kappa=N}\left(\frac{\mathcal{E}_\kappa d_{cv}\lambda_{15}b_{54}}{\Delta E_{cv^j}\Delta E_{cv_1}} + \frac{\mathcal{E}_\kappa d_{cv}\lambda_{46}b_{16}}{\Delta E_{cv^j}\Delta E_{cv_2}}\right)\left(\alpha_\kappa\beta_\kappa^j\right)\left(\sum_{\xi=1}^{\xi=N}\alpha_\xi\beta_\xi^j\right) + \sum_{\eta=1}^{\eta=N}\alpha_\eta^2\left(\frac{\mathcal{E}_\eta d_{v_1v_2}b_{54}\lambda_{46}}{\Delta E_{cv_1}\Delta E_{cv_2}} + \frac{\mathcal{E}_\eta d_{c_1c}b_{16}^{c_1v_2}\lambda_{46}}{\Delta E_{cc_1}\Delta E_{cv_2}}\right)\Bigg](\mathbf{s}\times\mathbf{k}),$$

$$\Delta H_{11}''' = 2\Bigg[\sum_{j=1}^{j=N}\sum_{\kappa=1}^{\kappa=N}\left(\frac{b_{54}\lambda_{15}\delta_{cv}}{\Delta E_{cv_1}\Delta E_{cv^j}} + \frac{b_{16}\lambda_{46}\delta_{cv}}{\Delta E_{cv_2}\Delta E_{cv^j}}\right)\alpha_\kappa\left(\beta_{\kappa+1}^j + \beta_{\kappa-1}^j\right)\left(\sum_{\xi=1}^{\xi=N}\alpha_\xi\beta_\xi^j\right)$$
$$+ \sum_{\eta=1}^{\eta=N}\left(\frac{b_{16}^{c_1v_2}\lambda_{46}\delta_{c_1c}}{\Delta E_{cc_1}\Delta E_{cv_1}}\right)\times\alpha_\eta(\alpha_{\eta+1}+\alpha_{\eta-1})\Bigg](\mathbf{s}\times\mathbf{k}). \quad \text{(D11)}$$

Finally, using Eq. (D9) the interfacial contribution to the SOC strength coming from the dominant $\Upsilon_{cv}^{t/b}$ term in Eq. (C2) has the form

$$\Delta H_{11}^{(I)} = 2\Bigg[\sum_{j=1}^{j=N}\left(\frac{b_{54}\lambda_{15}}{\Delta E_{cv^j}\Delta E_{cv_1}} + \frac{b_{16}\lambda_{46}}{\Delta E_{cv^j}\Delta E_{cv_2}}\right)\left(\Upsilon_{cv}^t\alpha_1\beta_1^j - \Upsilon_{cv}^b\alpha_N\beta_N^j\right)\left(\sum_{\xi=1}^{\xi=N}\alpha_\xi\beta_\xi^j\right)\Bigg](\mathbf{s}\times\mathbf{k}). \quad \text{(D12)}$$

Considering the limit where the applied electric field is zero, this term simplifies to

$$\Delta H_{11}^{(I)} = 2\left[\frac{b_{54}\lambda_{15}}{\Delta E_{g^1}\Delta E_{cv_1}} + \frac{b_{16}\lambda_{46}}{\Delta E_{g^1}\Delta E_{cv_2}}\right]\left(\Upsilon_{cv}^t\alpha_1\beta_1^1 - \Upsilon_{cv}^b\alpha_N\beta_N^1\right)(\mathbf{s}\times\mathbf{k}). \quad \text{(D13)}$$

[1] M. J. Hamer, J. Zultak, A. V. Tyurnina, V. Zólyomi, D. Terry, A. Barinov, A. Garner, J. Donoghue, A. P. Rooney, V. Kandyba, A. Giampietri, A. Graham, N. Teutsch, X. Xia, M. Koperski, S. J. Haigh, V. I. Fal'ko, R. V. Gorbachev, and N. R. Wilson, ACS Nano **13**, 2136 (2019).

[2] M. Brotons-Gisbert, D. Andres-Penares, J. Suh, F. Hidalgo, R. Abargues, P. J. Rodríguez-Cantó, A. Segura, A. Cros, G. Tobias, E. Canadell, P. Ordejón, J. Wu, J. P. Martínez-Pastor, and J. F. Sánchez-Royo, Nano Lett. **16**, 3221 (2016).

[3] N. Ubrig, E. Ponomarev, J. Zultak, D. Domaretskiy, V. Zólyomi, D. Terry, J. Howarth, I. Gutierrez Lezama, A. Zhukov, Z. Kudrynskyi, Z. Kovalyuk, A. Patanè, T. Taniguchi, K. Watanabe, R. Gorbachev, V. I. Fal'ko, and A. Morpurgo, Nat. Mater. **19**, 299 (2020).

[4] D. J. Terry, V. Zólyomi, M. J. Hamer, A. V. Tyurnina, D. Hopkinson, A. M. Rakowski, S. J. Magorrian, N. Clark, Y. M. Andreev, O. Kazakova, K. S. Novoselov, S. J. Haigh, V. I. Fal'ko, and R. V. Gorbachev, 2D Mater. **5**, 041009 (2018).

[5] G. W. Mudd, S. A. Svatek, L. Hague, O. Makarovsky, Z. R. Kudrynskyi, C. J. Mellor, P. H. Beton, L. Eaves, K. S. Novoselov, Z. D. Kovalyuk, E. Vdovin, A. J. Marsden, N. R. Wilson, and A. Patané, Adv. Mater. (Weinhien, Ger.) **27**, 3760 (2015).

[6] P. Kang, 2D Mater. **7**, 021002 (2020).

[7] Z. Kudrynskyi, J. Kerfoot, D. Mazumder, M. Greenaway, E. Vdovin, O. Makarovsky, Z. Kovalyuk, L. Eaves, P. Beton, and A. Patanè, Commun. Phys. **3**, 16 (2020).

[8] J. Zultak, S. Magorrian, M. Koperski, A. Garner, M. Hamer, E. Tóvári, K. Novoselov, A. Zhukov, Y. Zou, N. Wilson, S. Haigh, A. Kretinin, V. I. Fal'ko, and R. Gorbachev, Nat. Commun. **11**, 125 (2020).

[9] G. Mudd, S. Svatek, T. Ren, A. Patanè, O. Makarovsky, L. Eaves, P. Beton, Z. Kovalyuk, G. Lashkarev, Z. Kudrynskyi, and A. Dmitriev, Adv. Mater. (Weinhien, Ger.) **25**, 5714 (2013).

[10] H.-C. Chang, C.-L. Tu, K.-I. Lin, J. Pu, T. Takenobu, C.-N. Hsiao, and C.-H. Chen, Small **14**, 1802351 (2018).

[11] D. A. Bandurin, A. V. Tyurnina, L. Y. Geliang, A. Mishchenko, V. Zólyomi, S. V. Morozov, R. K. Kumar, R. V. Gorbachev, Z. R. Kudrynskyi, S. Pezzini, Z. D. Kovalyuk, U. Zeilter, K. S. Novoselov, A. Patanè, L. Eaves, I. V. Grigorieva, V. I. Fal'ko, A. K. Geim, and Y. Cao, Nat. Nanotechnol. **12**, 223 (2017).

[12] W. Li, S. Poncé, and F. Giustino, Nano Lett. **19**, 1774 (2019).

[13] P.-H. Ho, Y.-R. Chang, Y.-C. Chu, M.-K. Li, C.-A. Tsai, W.-H. Wang, C.-H. Ho, C.-W. Chen, and P.-W. Chiu, Acs Nano **11**, 7362 (2017).

[14] M. Zhou, S. Yu, W. Yang, W.-k. Lou, F. Cheng, D. Zhang, and K. Chang, Phys. Rev. B **100**, 245409 (2019).

[15] K.-H. Kim, H.-j. Kim, H. C. Koo, J. Chang, and S.-H. Han, Appl. Phys. Lett. **97**, 012504 (2010).

[16] M. Schultz, F. Heinrichs, U. Merkt, T. Colin, T. Skauli, and S. Løvold, Semicond. Sci. Technol. **11**, 1168 (1996).

[17] J. Hinz, H. Buhmann, M. SchLafer, V. Hock, C. Becker, and L. Molenkamp, Semiconductor science and technology **21**, 501 (2006).

[18] Z. Wang, D.-K. Ki, J. Y. Khoo, D. Mauro, H. Berger, L. S. Levitov, and A. F. Morpurgo, Phys. Rev. X **6**, 041020 (2016).

[19] S. Omar and B. J. van Wees, Phys. Rev. B **97**, 045414 (2018).

[20] C. Niu, G. Qiu, Y. Wang, Z. Zhang, M. Si, W. Wu, and P. D. Ye, Phys. Rev. B **101**, 205414 (2020).

[21] A. Manchon, H. Koo, J. Nitta, S. Frolov, and R. Duine, Nat. Mater. **14**, 871 (2015).

[22] D. Shcherbakov, P. Stepanov, S. Memaran, Y. Wang, Y. Xin, J. Yang, K. Wei, R. Baumbach, W. Zheng, K. Watanabe *et al.*, Sci. Adv. **7**, eabe2892 (2021).

[23] D. Liang and X. P. Gao, Nano Lett. **12**, 3263 (2012).

[24] R. van Gelderen and C. M. Smith, Phys. Rev. B **81**, 125435 (2010).

[25] K. Premasiri and X. P. Gao, J. Phys.: Condens. Matter **31**, 193001 (2019).

[26] I. Žutić, J. Fabian, and S. D. Sarma, Rev. Mod. Phys. **76**, 323 (2004).

[27] I. Zutic, J. Fabian, and S. D. Sarma, Acta Phys. Slovaca **57**, 567 (2007).

[28] E. A. de Andrada e Silva, G. C. La Rocca, and F. Bassani, Phys. Rev. B **55**, 16293 (1997).

[29] R. S. Calsaverini, E. Bernardes, J. C. Egues, and D. Loss, Phys. Rev. B **78**, 155313 (2008).

[30] R. Lassnig, Phys. Rev. B **31**, 8076 (1985).

[31] M. Kurpas, M. Gmitra, and J. Fabian, Phys. Rev. B **94**, 155423 (2016).

[32] A. Dankert and S. Dash, Nat. Commun. **8**, 16093 (2017).

[33] W. Zawadzki and P. Pfeffer, Semicond. Sci. Technol. **19**, R1 (2003).

[34] N. Kuroda and Y. Nishina, Solid State Commun. **34**, 481 (1980).

[35] S. J. Magorrian, V. Zólyomi, and V. I. Fal'ko, Phys. Rev. B **94**, 245431 (2016).

[36] S. J. Magorrian, *Theory of Electronic and Optical Properties of Atomically Thin Films of Indium Selenide* (Springer, Berlin, 2019).

[37] S. J. Magorrian, A. Ceferino, V. Zólyomi, and V. I. Fal'ko, Phys. Rev. B **97**, 165304 (2018).

[38] L. H. Thomas, Nature **117**, 514 (1926).

[39] The linear in wave vector SOC prescribed by the C_{3v} point group has the form $H_{SO}^{(1)} = i\alpha(k_- \mathbf{s}_+ - k_+ \mathbf{s}_-)$, where $k_\pm \equiv k_x \pm ik_y$ and $\mathbf{s}_\pm \equiv \frac{1}{2}(\mathbf{s_x} \pm i\mathbf{s_y})$. A higher-order invariant in wave vector k can be constructed replacing $k_\pm$ by $k_\pm^3$, therefore leading to a cubic SOC of the form $H_{SO}^{(3)} = -i\beta(k_-^3 \mathbf{s}_+ - k_+^3 \mathbf{s}_-) = 2\beta((k_x^3 - 3k_x k_y^2)\mathbf{s_y} - (3k_y k_x^2 - k_y^3)\mathbf{s_x})$.

[40] L. Gerchikov and A. Subashiev, Fiz. Tekh. Poluprovodn. **26**, 131 (1992) [Sov. Phys.–Semicond. **26**, 73 (1992)].

[41] R. Winkler, S. Papadakis, E. De Poortere, and M. Shayegan, *Spin-Orbit Coupling in Two-Dimensional Electron and Hole Systems*, Vol. 41 (Springer, Berlin, 2003).

[42] D. Kochan, S. Irmer, and J. Fabian, Phys. Rev. B **95**, 165415 (2017).

[43] J. Rigoult, A. Rimsky, and A. Kuhn, Acta Crystallogr., Sect. B: Struct. Crystallogr. Cryst. Chem. **36**, 916 (1980).

[44] G. Dresselhaus, Phys. Rev. **100**, 580 (1955).

[45] P. Pfeffer and W. Zawadzki, Phys. Rev. B **52**, R14332 (1995).

[46] Y. A. Bychkov and É. I. Rashba, Pis'ma Zh. Eksp. Teor. Fiz. **39**, 66 (1984) [JETP Lett. **39**, 78 (1984)].

[47] R. Winkler and U. Rossler, Phys. Rev. B **48**, 8918 (1993).

[48] M. Zhou, R. Zhang, J. Sun, W.-K. Lou, D. Zhang, W. Yang, and K. Chang, Phys. Rev. B **96**, 155430 (2017).

[49] J. P. Perdew, K. Burke, and M. Ernzerhof, Phys. Rev. Lett. **77**, 3865 (1996).

[50] G. Kresse and J. Furthmüller, Phys. Rev. B **54**, 11169 (1996).

[51] P. Li and I. Appelbaum, Phys. Rev. B **92**, 195129 (2015).

[52] Note that the SOC coefficients α, implied by the DFT results 18.6 meV Å and 32.3 meV Å for bilayer and trilayer, respectively, are somewhat larger than those predicted by the model presented in this work; this is due to the substantial underestimation of the band gap of InSe by DFT. We therefore base the parametrization of the model on GW results for bulk crystals.

[53] G. Dresselhaus and M. S. Dresselhaus, Phys. Rev. **140**, A401 (1965).

[54] S. J. Magorrian, V. Zólyomi, and V. I. Fal'ko, Phys. Rev. B **96**, 195428 (2017).

[55] D. Wang, W. Ju, T. Li, Q. Zhou, Y. Zhang, Z. Gao, D. Kang, H. Li, and S. Gong, J. Phys.: Condens. Matter **33**, 045501 (2020).

[56] D. V. Rybkovskiy, A. V. Osadchy, and E. D. Obraztsova, Phys. Rev. B **90**, 235302 (2014).

[57] A. V. Lugovskoi, M. I. Katsnelson, and A. N. Rudenko, Phys. Rev. Lett. **123**, 176401 (2019).

[58] V. Zólyomi, N. D. Drummond, and V. I. Fal'ko, Phys. Rev. B **89**, 205416 (2014).

[59] D. A. B. Miller, D. S. Chemla, T. C. Damen, A. C. Gossard, W. Wiegmann, T. H. Wood, and C. A. Burrus, Phys. Rev. Lett. **53**, 2173 (1984).

[60] A. Ceferino, K. W. Song, S. J. Magorrian, V. Zólyomi, and V. I. Fal'ko, Phys. Rev. B **101**, 245432 (2020).

[61] D. Pashov, S. Acharya, W. R. Lambrecht, J. Jackson, K. D. Belashchenko, A. Chantis, F. Jamet, and M. van Schilfgaarde, Comput. Phys. Commun. **249**, 107065 (2020).

[62] P.-O. Löwdin, J. Chem. Phys. **19**, 1396 (1951).

[63] P.-O. Löwdin, Int. J. Quantum Chem. **21**, 69 (2004).

[64] Y. Cao, A. Mishchenko, G. L. Yu, E. Khestanova, A. P. Rooney, E. Prestat, A. V. Kretinin, P. Blake, M. B. Shalom, C. Woods, J. Chapman, G. Balakrishnan, I. V. Grigorieva, K. S. Novoselov, B. A. Piot, M. Potemski, K. Watanabe, T. Taniguchi, S. J. Haigh, A. K. Geim *et al.*, Nano Lett. **15**, 4914 (2015).

[65] X. Cui, G.-H. Lee, Y. Kim, G. Arefe, P. Huang, C.-H. Lee, D. Chenet, X. Zhang, L. Wang, F. Ye, F. Pizzocchero, B. Jessen,

K. Watanabe, T. Taniguchi, D. Muller, T. Low, P. Kim, and J. Hone, Nat. Nanotechnol. **10**, 534 (2015).

[66] Z. R. Kudrynskyi, M. A. Bhuiyan, O. Makarovsky, J. D. G. Greener, E. E. Vdovin, Z. D. Kovalyuk, Y. Cao, A. Mishchenko, K. S. Novoselov, P. H. Beton, L. Eaves, and A. Patanè, Phys. Rev. Lett. **119**, 157701 (2017).

[67] W. Li and F. Giustino, Phys. Rev. B **101**, 035201 (2020).

[68] T. Koga, J. Nitta, T. Akazaki, and H. Takayanagi, Phys. Rev. Lett. **89**, 046801 (2002).

[69] F. G. Pikus and G. E. Pikus, Phys. Rev. B **51**, 16928 (1995).

[70] S. Hikami, A. I. Larkin, and Y. Nagaoka, Prog. Theor. Phys. **63**, 707 (1980).

[71] Y. Araki, G. Khalsa, and A. H. MacDonald, Phys. Rev. B **90**, 125309 (2014).

[72] B. L. Altshuler, D. Khmel'nitzkii, A. I. Larkin, and P. A. Lee, Phys. Rev. B **22**, 5142 (1980).

[73] B. L. Altshuler, A. Aronov, D. Khmel'nitzkii, A. I. Larkin, and P. A. Lee, Zh. Eksp. Teor. Fiz. **81**, 768 (1981) [JETP Lett. **54**, 411 (1981)].

[74] S. Takasuna, J. Shiogai, S. Matsuzaka, M. Kohda, Y. Oyama, and J. Nitta, Phys. Rev. B **96**, 161303(R) (2017).

[75] K. Premasiri, S. K. Radha, S. Sucharitakul, U. R. Kumar, R. Sankar, F.-C. Chou, Y.-T. Chen, and X. P. A. Gao, Nano Lett. **18**, 4403 (2018).

[76] J. Zeng, S.-J. Liang, A. Gao, Y. Wang, C. Pan, C. Wu, E. Liu, L. Zhang, T. Cao, X. Liu, Y. Fu, Y. Wang, K. Watanabe, T. Taniguchi, H. Lu, and F. Miao, Phys. Rev. B **98**, 125414 (2018).

[77] R. J. Elliott, Phys. Rev. **96**, 266 (1954).

[78] Y. Yafet, J. Phys. C: Solid State Phys. **14**, 1 (1963).

[79] S. V. Iordanskii, Y. B. Lyanda-Geller, and G. E. Pikus, Pis'ma Zh. Eksp. Teor. Fiz. **60**, 199 (1994) [Sov. J. Exp. Theor. Phys. Lett. **60**, 206 (1994)].

[80] W. Knap, C. Skierbiszewski, A. Zduniak, E. Litwin-Staszewska, D. Bertho, F. Kobbi, J. L. Robert, G. E. Pikus, F. G. Pikus, S. V. Iordanskii, V. Mosser, K. Zekentes, and Y. B. Lyanda-Geller, Phys. Rev. B **53**, 3912 (1996).

[81] L. E. Golub, Phys. Rev. B **71**, 235310 (2005).

[82] M. M. Glazov and L. Golub, Semiconductors **40**, 1209 (2006).

[83] M. Dyakonov and V. Kachorovskii, Fiz. Tekh. Poluprovodn. **20**, 178 (1986) [Sov. Phys.-Semicond. **20**, 110 (1986)].

[84] M. Dyakonov and V. Perel, Fiz. Tverd. Tela **13**, 3581 (1971) [Sov. Phys.–Solid State **13**, 3023 (1972)].

[85] M. Zhou, D. Zhang, S. Yu, Z. Huang, Y. Chen, W. Yang, and K. Chang, Phys. Rev. B **99**, 155402 (2019).

[86] F. T. Vas'ko, Pis'ma Zh. Eksp. Teor. Fiz. **30**, 574 (1979) [Sov. J. Exp. and Theor. Phys. Lett. **30**, 541 (1979)].

[87] S. Novakov, B. Jariwala, N. M. Vu, A. Kozhakhmetov, J. A. Robinson, and J. T. Heron, ACS Applied Materials & Interfaces **13**, 13744 (2021).